

DEPENDENCE OF ELASTIC NONLINEARITY ON ALIGNED INHOMOGENEITIES

by

©Jacob Edward Newman

A Dissertation submitted to the School of Graduate Studies in partial fulfillment of
the requirements for the degree of

Masters of Science (Geophysics)
Department of Earth Sciences

Memorial University of Newfoundland

July 8, 2021

St. John's

Newfoundland

Abstract

The nonlinear elasticity of geomaterials is a prominent indicator of the materials' internal structure (micro-fractures, grain-to-grain boundaries, etc.), both microscopically and macroscopically. Dynamic acousto-elastic testing (DAET) has become a standard tool to assess the nonlinear elasticity of materials. Here, we use a transient wave variation of DAET (TW-DAET) to evaluate whether this type of testing can (1) distinguish the presence of varying types of inhomogeneities and (2) determine the direction in which said inhomogeneities align. We explore two main types of inhomogeneities with TW-DAET; micro-fracturing in sandstone samples (which we attempt to induce via freeze-thaw cycles) and embedded objects within an elastically linear background cement. The sandstone results remain largely inconclusive though evidence for a potential two-mechanism (one increasing and one decreasing nonlinearity) system is presented in a subset of the data. We observe the presence and alignment of inhomogeneities for a sub-set of the cement samples we examine with TW-DAET. We also find evidence for a potential dependence of the nonlinearity on the relative sizes of the probe's wavelength and the spatial characteristics of the inhomogeneities.

Acknowledgements

I want to start by thanking my co-supervisors, Dr. Alison Malcolm and Dr. Kris Poduska, with whom I have worked in different capacities for four years now. Their scientific criticisms have gone a long way over the years and have shaped this project, as well as I, into what they are today.

I would also like to acknowledge the skills I have gained from the respective courses given by Dr. Kim Welford, Dr. Colin Farquharson and Dr. James Munroe.

I am grateful to Dr. Andrey Melnikov for his help with the theory section of this project and Dr. Somayeh Khajehpour Tadavani for her help with laboratory experiments.

I greatly appreciate the many friends I have made throughout my time at Memorial University for their educational and emotional support. In particular, Miguel Shano and Steven Lethbridge, whom I have worked closely with since our second-year undergraduate, and my girlfriend Chelsea Ryan, who was always there when nothing in the laboratory seemed to be working (not an isolated occurrence).

Finally, I would like to thank the following funding sources: Chevron Canada, the Natural Sciences and Engineering Research Council, and Memorial University's School of Graduate Studies.

Contents

Abstract	ii
Acknowledgments	iii
List of Tables	vi
List of Figures	vii
List of Abbreviations	xv
List of Symbols	xvi
1 Introduction and Overview	1
1.1 Elastic Nonlinearity	1
1.1.1 Classical Elastic Nonlinearity	1
1.1.2 Non-Classical Elastic Nonlinearity	5
1.2 Elastic Nonlinearity Experiments	10
1.2.1 Dynamic Acousto-elastic Testing (DAET)	11
2 Methodology	14
2.1 Transient Wave Dynamic Acousto-elastic Testing (TW-DAET)	14
2.2 Fracturing Work Flow	21

2.2.1	Freeze-thaw Fracturing	21
2.2.2	Cement Models	25
3	Experimental Results	30
3.1	Freeze-thaw Fracturing Results	31
3.1.1	Tap Water	32
3.1.2	Salt Saturated Water	36
3.2	Cement Model Results	39
3.2.1	Homogeneous Cement (CH1)	40
3.2.2	Cement with Thick Sand (CS1)	44
3.2.3	Cement with Thin Sand 1 (CS2)	46
3.2.4	Cement with Thin Sand 2 (CS2)	48
3.2.5	Cement with Metal Rods (CR1)	50
3.2.6	Cement with Copper Wires 1 (CC1)	52
3.2.7	Cement with Copper Wires 2 (CC2)	54
4	Discussion	56
4.1	Freeze-thaw Fracturing	56
4.2	Cement Models	60
4.2.1	Expected Nonlinearity Increases	60
4.2.2	Unconsolidated Sand Models	63
4.2.3	Metal Rod/Wire Models	66
5	Conclusions and Future Work	71
	Bibliography	75

List of Tables

List of Figures

1.1	Different types of elastic stress-strain regimes. (A) linear, (B) classical nonlinear and (C) non-classical nonlinear (visco-elastic).	2
1.2	Conceptional model proposed by Sens-Schönfelder et al. (2019) to explain the dynamics observed in elastic modulus when a granular material is subject to different degrees of strain. From Sens-Schönfelder et al. (2019) with © The Author(s) 2018. Published by Oxford University Press on behalf of The Royal Astronomical Society.	8
1.3	(a) Dynamic acousto-elastic data from the testing of a sandstone sample collect by Riviére et al. (2013). (b) Forward modelled data to match the experimental results calculated with the elastic modulus model proposed by Sens-Schönfelder et al. (2019) given in equation (1.16). From Sens-Schönfelder et al. (2019) with © The Author(s) 2018. Published by Oxford University Press on behalf of The Royal Astronomical Society.	9
2.1	The transient wave dynamic acousto-elastic testing (TW-DAET) experimental setup we employ.	16
2.2	We show three transmission delays to depict how the probe (blue) interacts with different pump (red) phases in our samples as we change the transmission delay.	18

2.3	Shown here is the probe time delay calculation process for three transmission delays. Row one shows the recorded waveforms ($S_{1,2,3}$) and the calculated perturbed probe (S_4). Row two shows the cross-correlation function along with the parabolic fit for the unperturbed and perturbed probe signals (i.e., $S_4 \star S_1$). Note that the parabolic fit maximum (red square) corresponds to the probe time delay at that particular transmission delay (plotted on the y-axis in row three).	19
2.4	Here we show the pump-probe orientation diagrams employed during TW-DAET. Orientation one (left) defines the pump and probe propagation directions parallel to x and y, respectively, with each wave, polarized vice-versa. Orientation two (right) defines propagation directions of the pump and probe in x and z, respectively, again with each wave polarized vice-versa.	20
2.5	Preliminary time delay results from a sandstone sample. Note the inherent difference seen between orientation one (red) and orientation two (blue).	20
2.6	Relative change in water volume (%) as external temperature progresses through its freezing point of 0° C. From Kharseh (2018) used under the terms of the Creative Commons Attribution 4.0 International License (http://creativecommons.org/licenses/by/4.0/).	22
2.7	Weights of six sandstone samples (NS1-6) at each stage of the tap water freeze-thaw process with and without the vise (note that we detached the vise during the weighing process). The average water weight we add during the saturation process is 61 g, and the average we remove during drying is 69 g.	23

2.8	Flow diagram depicting the freeze-thaw process: 1. Sample saturation with tap or salt-saturated water in a vacuum chamber; 2. Sample freezing with and without the vise (we complete the entire workflow twice with each sample); 3. Sample drying in an oven.	24
2.9	Magnified image of the sand we use to create samples CS1-3.	27
2.10	Schematic depicting the six prismatic inhomogeneous cement samples on which we complete TW-DAET. Samples A, B, and C consist of embedded unconsolidated sand layers of varying thickness and separation. The inhomogeneities in samples D, E, and F consist of two types of metallic cylinders (metal rods; D and copper wires; E and F) again with varying diameter and separation. Note that schematic diagrams are not to scale.	29
2.11	Shown are three inhomogeneous cement samples before the addition of the top layer of cement. Left: Thick unconsolidated sand layers; Middle: metal rods; Right: ten copper wires separated by five millimetres.	29
3.1	A: schematic depicting the three main components of time delays at their distinct frequencies (1, 2 and 3). Schematics depicting the addition of components at frequencies one and two (B) and frequencies one and three (C). Examples of time delays with a clear presence of frequencies one and two (D; NS5) and frequencies one and three (E; CC1).	31
3.2	Time delay results from sample NS3 orientation one (top) and orientation two (bottom). We compare initial time delays (blue) to the post-freeze workflow time delays (red) for both orientations.	33

3.9 Time delay results for the homogeneous cement sample in orientation two. The average trend of four runs is shown (dashed line) with ± 2 standard deviations highlighted by the shaded region.	43
3.10 Orientation one time delay results for the cement sample with three thick sand layers (red) compared with the homogeneous cement time delays (blue). The average trend of three runs (four runs) is shown (dashed line) with ± 2 standard deviations highlighted by the shaded region.	44
3.11 Orientation two time delay results for the cement sample with three thick sand layers (red) compared with the homogeneous cement time delays (blue). The average trend of four runs is shown (dashed line) with ± 2 standard deviations highlighted by the shaded region. . . .	45
3.12 Orientation one time delay results for the cement sample with three thin sand layers (red) compared with the homogeneous cement time delays (blue). The average trend of three runs (four runs) is shown (dashed line) with ± 2 standard deviations highlighted by the shaded region.	46
3.13 Orientation two time delay results for the cement sample with three thin sand layers (red) compared with the homogeneous cement time delays (blue). The average trend of four runs is shown (dashed line) with ± 2 standard deviations highlighted by the shaded region. . . .	47
3.14 Orientation one time delay results for the cement sample with seven thin sand layers (red) compared with the homogeneous cement time delays (blue). The average trend of five runs (four runs) is shown (dashed line) with ± 2 standard deviations highlighted by the shaded region.	48

3.15 Orientation two time delay results for the cement sample with seven thin sand layers (red) compared with the homogeneous cement time delays (blue). The average trend of three runs (four runs) is shown (dashed line) with ± 2 standard deviations highlighted by the shaded region.	49
3.16 Orientation one time delay results for the cement sample with metal rods (red) compared with the homogeneous cement time delays (blue). The average trend of three runs (four runs) is shown (dashed line) with ± 2 standard deviations highlighted by the shaded region.	50
3.17 Orientation two time delay results for the cement sample with metal rods (red) compared with the homogeneous cement time delays (blue). The average trend of four runs is shown (dashed line) with ± 2 standard deviations highlighted by the shaded region.	51
3.18 Orientation one time delay results for the cement sample with copper wires separated at 5 mm (red) compared with the homogeneous cement time delays (blue). The average trend of five runs (four runs) is shown (dashed line) with ± 2 standard deviations highlighted by the shaded region.	53
3.19 Orientation two time delay results for the cement sample with copper wires separated at 5 mm (red) compared with the homogeneous cement time delays (blue). The average trend of four runs is shown (dashed line) with ± 2 standard deviations highlighted by the shaded region. . .	53

3.20 Orientation one time delay results for the cement sample with copper wires separated at 10 mm (red) compared with the homogeneous cement time delays (blue). The average trend of five runs (four runs) is shown (dashed line) with ± 2 standard deviations highlighted by the shaded region.	55
3.21 Orientation two time delay results for the cement sample with copper wires separated at 10 mm (red) compared with the homogeneous cement time delays (blue). The average trend of five runs (four runs) is shown (dashed line) with ± 2 standard deviations highlighted by the shaded region.	55
4.1 Time delay trends from NS5 over iterations (rows) of the salt-freeze workflow in orientation one and two (left and right columns, respectively). Comparison of time delays at the current iteration (solid red) with initial time delays (blue) and time delays of the previous iteration (dashed red). Red and blue fill represent decreases and increases, respectively, relative to the previous iteration.	59
4.2 Schematic depicting how the pump wave (red) interacts with horizontal unconsolidated sand layers in orientation one (left) and orientation two (right).	62
4.3 Schematic depicting how the pump wave (red) interacts with a network of Cu wires in orientation one (left) and orientation two (right). . . .	62
4.4 A Schematic depicting the three unconsolidated sand layer cement samples; CS1 (A), CS2 (B) and CS3 (C). Note that schematic diagrams are not to scale.	63
4.5 Orientation one mean time delay trend comparisons between sand samples (red) and homogeneous cement (blue).	64

4.6	Orientation two mean time delay trend comparisons between sand samples (red) and homogeneous cement (blue).	65
4.7	A Schematic depicting the three metal cylinder cement samples; CR1 (D), CC1 (E) and CC2 (F). Note that schematic diagrams are not to scale.	66
4.8	Orientation one mean time delay trend comparisons between metal cylinder samples (red) and homogeneous cement (blue).	68
4.9	Orientation two mean time delay trend comparisons between metal cylinder samples (red) and homogeneous cement (blue).	70

List of Abbreviations

DAET	Dynamic acousto-elastic testing
TW-DAET	Transient wave dynamic acousto-elastic testing
<i>pr</i>	Probe
<i>pu</i>	Pump
O1	Pump-probe orientation one
O2	Pump-probe orientation two
S/N	Signal-to-noise ratio

List of Symbols

\mathbf{S}	Stress tensor
$\boldsymbol{\epsilon}$	Strain tensor
\mathbf{u}	Displacement gradient
ρ_0	Density
V_{s_0}	Initial shear velocity
V_s	Perturbed shear velocity
λ	Wavelength
μ	Shear modulus
A, B, C	Third-order elastic constants (Landau & Lifshitz (1986))
D	Fourth-order elastic constant (Hamilton et al. (2004))
\mathbf{E}^k	Lagrangian strain tensor
I_k	Strain invariant
W	Strain energy density
β	Quadratic coefficient of nonlinearity
δ	Cubic coefficient of nonlinearity
SD	Standard deviation
\bar{x}	Mean
$^\circ \text{C}$	Degrees Celsius

Chapter 1

Introduction and Overview

1.1 Elastic Nonlinearity

1.1.1 Classical Elastic Nonlinearity

Introduction

Elasticity focuses on a material's response following the application of varying stress (load). Specifically, elasticity refers to when a material's stress response-strain elastically returns to some unloaded state after loading. In other words, the loading of the material does not result in any permanent damage.

Both linear and nonlinear elastic materials will restore to some unloaded state elastically. The difference between the two regimes manifests itself in the stress-strain relationship of a material. If this relationship is linear (figure 1.1 A), i.e., the strain is linearly proportional to the applied stress, the material is said to exhibit linear elasticity. If this relationship is more complex (e.g., quadratic), the material is said to exhibit nonlinear elasticity (figure 1.1 B). Landau & Lifshitz (1986) describes this

nonlinear relationship by expanding the elastic energy of the system as a power series with respect to the strain tensor under the small deformations approximation. We will discuss this theory in further detail in section (1.1.1). The third elasticity regime presents itself in numerous experimental observations that differ from the classical theory of nonlinearity. This nonlinear behaviour has been broadly dubbed non-classical nonlinearity compared to the classical theory proposed by Landau & Lifshitz (1986). This more phenomenological branch of nonlinear elasticity is prevalent in micro-inhomogeneous materials such as rocks (Riviére et al. (2013)), concrete (Scalerandi et al. (2018)), bones (Renaud et al. (2008)), damaged metals (Haupert et al. (2014)), and composites (Delrue & Van Den Abeele (2012)). The stressing of these materials leads to several phenomena, some well-understood, some not so well-understood, such as stress-strain hysteresis (figure 1.1 C), end-point memory and the slow dynamical recovery of a material's elastic parameters (Riviére et al. (2013)).

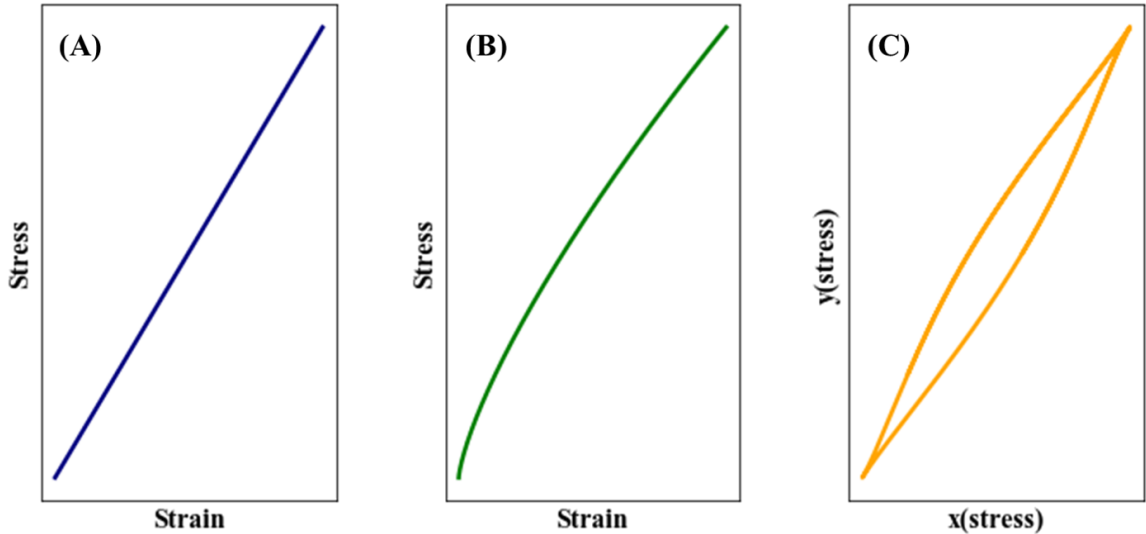


Figure 1.1: Different types of elastic stress-strain regimes. (A) linear, (B) classical nonlinear and (C) non-classical nonlinear (visco-elastic).

Theory

As we stated above, the classical nonlinear elasticity theory presented by Landau & Lifshitz (1986) starts with the strain energy density (W ; a function that accounts for a potential energy stored in a deformed material (Slawinski (2018))), which can be expanded with respect to three independent invariants

$$I_k = \text{tr}(\mathbf{E}^k), \quad k = 1, 2, 3, \quad (1.1)$$

where

$$\mathbf{E} = \frac{1}{2}(\epsilon_{ij} + \epsilon_{ji} + \sum_k \epsilon_{ki}\epsilon_{kj}). \quad (1.2)$$

This project's experiments employ shear wave transducers only; we, therefore, limit our theoretical development to the transverse wave case. Considering an isotropic solid under pure shear deformation, the strain energy density, up to cubic order, is given by

$$W = \mu I_2 + \frac{1}{3}AI_3 + DI_2^2, \quad (1.3)$$

where μ is the shear modulus, A is one of the third-order elastic constants introduced by Landau & Lifshitz (1986) and D is the fourth-order elastic constant derived by Hamilton et al. (2004). We observe no I_1 dependence in equation (1.3) as I_1 is defined by the strain induced by compressional forces. Differentiating with respect to the strain in each direction gives the Second Piola-Kirchhoff stress tensor

$$\mathbf{S} = \frac{\partial W}{\partial \mathbf{E}}. \quad (1.4)$$

Zabolotskaya et al. (2004) gives a lengthy derivation for the three-dimensional pure shear deformation stress tensor. Here we restrict our shear motion as a linearly po-

larized plane shear wave travelling in the y-direction and polarized in the x-direction, such as the probe wave in orientation one (section 2.1). This simplification results in a stress tensor

$$S_{xy} = \mu \frac{\partial u_x}{\partial y} + (\mu + \frac{A}{2} + D) \left(\frac{\partial u_x}{\partial y} \right)^3. \quad (1.5)$$

Landau & Lifshitz (1986) give the general equation of motion

$$\rho_0 \frac{\partial^2 u}{\partial t^2} = \frac{\partial S_{xy}}{\partial y}, \quad (1.6)$$

into which we substitute equation (1.5) which yields ($u_x \rightarrow u$)

$$\rho_0 \frac{\partial^2 u}{\partial t^2} = \mu \frac{\partial^2 u}{\partial y^2} + \gamma \frac{\partial}{\partial y} \left(\frac{\partial u}{\partial y} \right)^3, \quad (1.7)$$

where

$$\gamma = \mu + \frac{1}{2}A + D. \quad (1.8)$$

After some rearrangement and using the fact that $\mu = \rho_0 V_{s_0}^2$ we arrive at

$$\frac{\partial^2 u}{\partial t^2} = V_{s_0}^2 \frac{\partial^2 u}{\partial y^2} \left[1 + \left(\frac{6\mu + 3A + 6D}{2\mu} \right) \left(\frac{\partial u}{\partial y} \right)^2 \right], \quad (1.9)$$

which we can re-write as

$$\frac{\partial^2 u}{\partial t^2} = V_s^2 \frac{\partial^2 u}{\partial y^2}, \quad (1.10)$$

where

$$V_s^2 = V_{s_0}^2 \left[1 + \left(\frac{6\mu + 3A + 6D}{2\mu} \right) \left(\frac{\partial u}{\partial y} \right)^2 \right]. \quad (1.11)$$

One can see that the normalized difference between the velocities $V_{s_0}^2$ and V_s^2 will give

a measure of nonlinearity, i.e.,

$$\frac{V_s^2 - V_{s_0}^2}{V_{s_0}^2} = \left(\frac{6\mu + 3A + 6D}{2\mu} \right) \left(\frac{\partial u}{\partial y} \right)^2. \quad (1.12)$$

From the above derivation and explanation, it becomes clear that the higher-order elastic constants (A and D) quantify the amount of elastic nonlinearity. These elastic constants are often amalgamated into one nonlinearity coefficient β , i.e.,

$$\beta = \left(\frac{6\mu + 3A + 6D}{2\mu} \right) \quad (1.13)$$

Therefore, any set of experiments to test the elastic nonlinearity should derive the nonlinearity coefficient(s), a material property. As shown in (Gallot et al. (2014)), the nonlinearity coefficient(s) is not trivial to derive due to the necessary knowledge of the strain distribution. Thus it is often convenient to examine an indirect indicator of elastic nonlinearity: the local change in sound speed induced by an external stress (or strain).

The difference in velocity shown in equation (1.12) is analogous to the time delay difference we measure with our experimental setup as the distance the wave travels does not change. We discuss our measurement protocol in detail in section (2.1) and therefore acts as an indirect indication of the material, classical elastic nonlinearity, as desired.

1.1.2 Non-Classical Elastic Nonlinearity

The experimental methodology for this project aims to measure the classical non-linearity of different materials. For completeness, we give a brief summary of non-classical elastic nonlinearity.

Phenomena such as the generation of amplitude dependent higher harmonics and sidebands (Van Den Abeele et al. (2021); Baccouche et al. (2017)), stress-strain relationships ruled by multivariate hysteretic functions, end-point memory (Zinszner et al. (1997)), fast and slow conditioning and subsequent log-t recovery (Bentahar et al. (2006); TenCate et al. (2004); Johnson & Sutin (2005)) are observed in experiments on both solid materials with complex micro-inhomogeneous structures and soft solid materials. These behaviours prove to be insufficiently described by the classical elastic nonlinearity we discuss in section (1.1.2). Take for example a stress-strain relationship modelled by complex hysteresis loops. Here there is a dependence that exists between the applied stress and the resulting sign of the strain rate. In no way can equation (1.10) explain this dependence; therefore, we must append this equation with an additional term(s), yielding

$$\frac{\partial^2 u}{\partial t^2} = V_{s_0}^2 \frac{\partial^2 u}{\partial y^2} \left[1 + \left(\frac{6\mu + 3A + 6D}{2\mu} \right) \left(\frac{\partial u}{\partial y} \right)^2 \right] + H \left[\epsilon, \text{sign} \left(\frac{\partial \epsilon}{\partial t} \right) \right]. \quad (1.14)$$

The function H , which is dependent on both strain and the sign of the strain rate, describes the hysteretic nonlinearity of a material. In practice, deriving H would follow from the forward modelling of experimental data (Delsanto & Scalerandi (2003); Shkerdin & Glorieux (2009); Gusev et al. (2003)).

Guyer & Johnson (1999) summarize the different contributions of elastic nonlinearity for four materials: water, copper, rock and PZT5, a ceramic composed of lead, zirconate and titanate used as an acoustic source. They break their results down into the relative strengths of each of the terms of the wave equation, with an addition category: slow dynamics, which is another typical characteristic of non-classical elastic nonlinearity. A summary of these results are shown in table (1.1).

Sens-Schönfelder et al. (2019) propose a conceptional model based on the friction

Table 1.1: Relative strengths (β and δ) and indication of appearance (H) of terms of the nonlinear wave equation and appearance of slow dynamics for water, copper, rock, and PZT5 (after Guyer & Johnson 1999)

	β	δ	H	Slow dynamics
Water	6	36	No	No
Copper	7	49	No	No
Rock	10^3	10^6	Yes	Yes
PZT5	4-5	10^4	No	Yes

of internal surfaces that aims to define the variation of the elastic modulus for a sandstone sample, collected experimentally by Rivière et al. (2013) (figure 1.3a). Their model aims to give a physical definition for the hysteretic term in equation (1.14). Four physically distinct terms define the proposed modulus, which describe the different aspects of figure (1.2)

$$M = M_0 + \Delta M_1 + \Delta M_c + \Delta M_s; \quad (1.15)$$

$$M = M_0 - A\epsilon(t) + B\left(\exp\left[\frac{\epsilon(t)^2}{2w^2}\right] - 1\right) - CN(t). \quad (1.16)$$

Here the linear strain term accounts for the decrease in modulus with the application of extensional stress and the increase in modulus with application of compressional stress. This term is scaled by the material factor A (different from the third-order elastic constant proposed by Landau & Lifshitz (1986)). A quadratic strain dependence characterizes the next term; this term accounts for the decrease in modulus when internal boundaries are subject to shears force. There is a degree of correlation between the surface roughness on either side of a micro-fracture. When there are no shear forces, the two sides of a micro-fracture fit together like puzzle pieces, giving them more strength and increasing the modulus of the material. When these micro-fractures are subject to shearing, the roughness correlation is reduced, which decreases

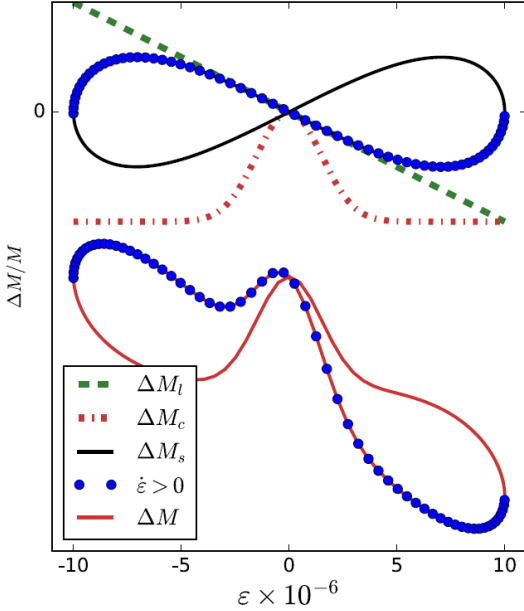


Figure 1.2: Conceptual model proposed by Sens-Schönfelder et al. (2019) to explain the dynamics observed in elastic modulus when a granular material is subject to different degrees of strain. From Sens-Schönfelder et al. (2019) with © The Author(s) 2018. Published by Oxford University Press on behalf of The Royal Astronomical Society.

the strength of the sample, which manifests in a decrease of the elastic modulus (Sens-Schönfelder et al. (2019)). This term is proportional to the inverse of the width of the approximately Gaussian modulus distribution (dashed red line in figure 1.2). The last term in equation (1.16) controls the hysteresis and conditioning of the modulus and is proportional to the average number density of damaged micro-connections ($N(t)$) and the scaling factor C . The synthetic data (figure 1.3b) generated using the above model matches the experimental data (figure 1.3a) sufficiently, thus validating the model to some degree.

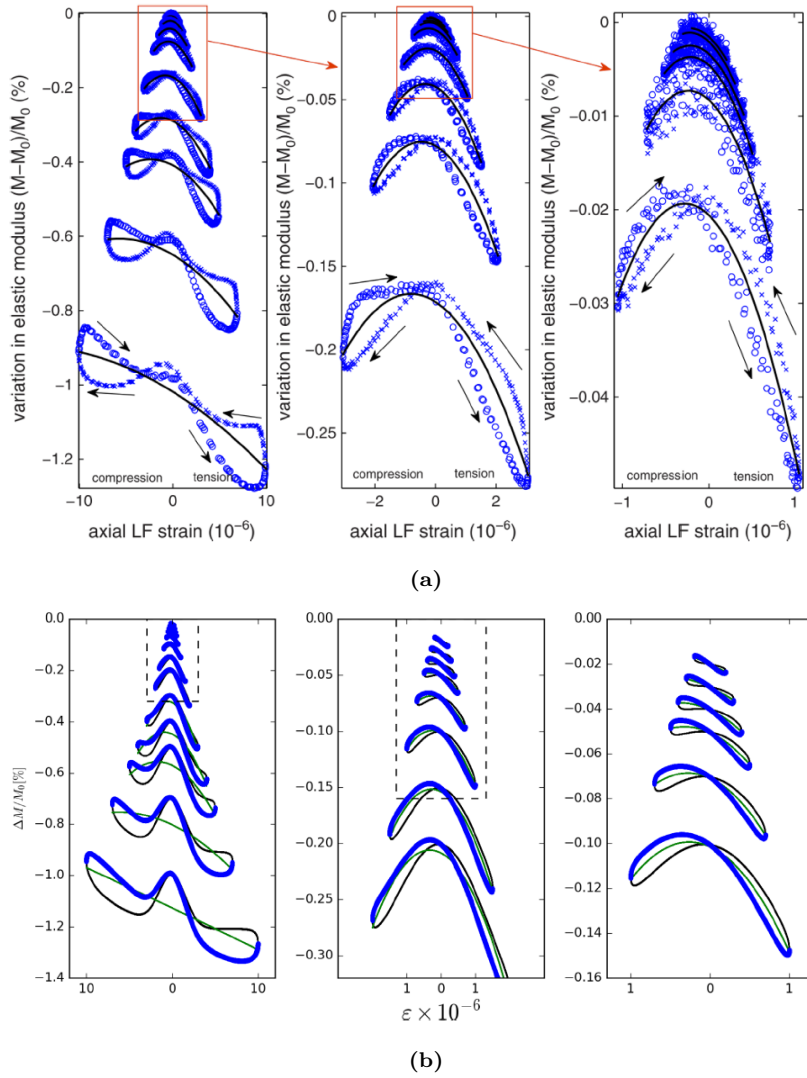


Figure 1.3: (a) Dynamic acousto-elastic data from the testing of a sandstone sample collect by Riviére et al. (2013). (b) Forward modelled data to match the experimental results calculated with the elastic modulus model proposed by Sens-Schönfelder et al. (2019) given in equation (1.16). From Sens-Schönfelder et al. (2019) with © The Author(s) 2018. Published by Oxford University Press on behalf of The Royal Astronomical Society.

1.2 Elastic Nonlinearity Experiments

Three classes of elastic nonlinearity experiments are defined based on the frequency of the applied load. Purely static experiments became the first class of elastic nonlinearity experiments in the early 1900s. These experiments aim to derive the effect a static load has on the thermodynamic properties of a material (Bridgman (1912)).

With the development of resonance spectroscopy (Birch (1937)) and ultrasonic transducer technology (Pellam & Galt (1946)), elastic nonlinearity became increasingly dynamic (in terms of the applied strain fields). Quasi-static experiments (Winkler & Liu (1995); Winkler & McGowan (2004)) refer to a class in which a step-wise function defines the uniaxial or hydrostatic pressure/stress applied. These experiments are still equivalent to zero-frequency measurements (Rivi  re et al. (2016)), their quasi-static nature stemming from the step-wise change in stress/pressure. With each step in applied load, the wave speed is measured, thus deriving the former's effect on the latter.

The third class of elastic nonlinearity experiments replaces the step-wise function of applied load with a low-frequency strain modulation. The extensively developed pump-probe scheme appropriate for this class of experiments is known in the literature as dynamic acousto-elastic testing (DAET). DAET involves a low-frequency, high-amplitude pump wave that perturbs the strain field within a material. We simultaneously measure this perturbation through the velocity change of a high-frequency, low-amplitude probe wave (Renaud et al. (2009)).

Here, we employ a type of DAET experiment first developed by Gallot et al. (2014) for deriving the nonlinear coefficients (β and δ) of a sandstone sample and subsequently used by Rusmanugroho et al. (2019) to model the effect of micro-fractures and by Khajehpour Tadavani et al. (2020) to experimentally derive the effect of ambient humidity. We continue our discussion on this experimental scheme briefly in

section (1.2.1) and extensively in chapter (2).

1.2.1 Dynamic Acousto-elastic Testing (DAET)

As we point to above, dynamic acousto-elastic testing (DAET) employs two dynamic fields known as the pump and probe. The pump is generally high-amplitude, resulting in large enough strain values to perturb the material's elastic properties in which it propagates. Conversely, the probe acts as a measuring tool comparing its time-of-flight (velocity), or other properties, across the sample with and without the pump wave.

DAET experiments employ different types of waves (compressional, stress, surface, etc.) for the pump and probe, depending on what the experiment aims to analyze. The probe's setup can involve one transducer that acts as the source and receiver (pulse-echo) or two transducers, one acting as a wave source and another situated on the opposite face working as a receiver (transmission). In both cases, the source can be either a compressional or a shear wave. A significant distinction between types of DAET comes with the choice of pump wave. Classically, DAET defines a standing wave pump field to perturb the elastic parameters of the sample. This characteristic is achieved by measuring and calculating the sample's resonance parameters and setting the pump transmission to match them; once the model is in resonance, the probe transmission proceeds. However, a standing wave pump can sometimes present a problem, as bringing the medium into resonance is not always possible. This complication leads to the choice of using a transient wave (compressional or shear) for the pump field (the method this project employs). This setup mirrors the probe transmission case; one transducer acts as a source and another, immediately opposite, as a receiver.

In the following two subsections (1.2.1 and 1.2.1), we present examples of both

types of DAET (standing wave and transient wave) from the literature.

Classic (standing wave)

The literature on classic (standing wave) DAET is becoming increasingly expansive. For this reason, we present a limited number of examples where standing wave DAET is performed.

An early example of implementing a wave coupling technique, similar to DAET, is given by Gremaud et al. (1987) in which they observe the formation of hysteresis curves within trends of linear attenuation and velocity as a function of applied stress.

Renaud et al. (2009) later refine the DAET design to a setup that is analogous to what is currently most commonly used. They use this implementation to derive the elastic nonlinearity coefficients of cracked and un-cracked Pyrex plates, demonstrating its practical and relatively simple application.

Renaud et al. (2012) report preliminary DAET results for eleven room-dry rock samples (hard and soft rock). They find that the nonlinear responses are markedly different for varying rock types, ultimately facilitating the physical interpretation of DAET aspects.

Scaleraudi et al. (2015) present an extensive computational investigation of the validity of DAET for measuring nonlinear elasticity. They find that although DAET is nuanced, it is faster to implement without sacrificing accuracy than other nonlinear techniques such as static acousto-elastic testing.

Transient Wave

Gallot et al. (2014) first develop the pump-probe nonlinear testing scheme in which the pump is a transient wave rather than a standing wave. They derive a fourth-order elastic model to relate the changes in elasticity to the pump strain components, which

they use to recover a sandstone sample's quadratic and cubic nonlinear parameters.

TenCate et al. (2016) subsequently use TW-DAET to explore the effect of crack orientation on the nonlinear response of a sandstone sample. They find preliminary evidence to suggest crack orientation partially affects the nonlinear response they record. We consider this project to be an extension of their work.

Hayes et al. (2018) examine the result of TW-DAET on sandstone samples as a function of uniaxial stress. They attempt to use the nonlinear effect to measure the opening and closing of aligned microfractures.

Rusmanugroho et al. (2019) later model TW-DAET and find that the nonlinear response is most significant when the particle motion of the pump is parallel with the normal of the crack face, resulting in a considerable magnitude crack dilation.

Khajehpour Tadavani et al. (2020) test what effect ambient humidity has on the TE-DAET response of a sandstone sample. They find that the pump more effectively softens the sandstone in humidified environments, leading to an increased nonlinear response.

Chapter 2

Methodology

2.1 Transient Wave Dynamic Acousto-elastic Testing (TW-DAET)

The nonlinear testing method we employ for this work follows a pump-probe dynamic acousto-elastic testing design in which the perturbation field (i.e. the pump) is a transient wave (section 1.2.1). As we discuss in section (1.1.2), any experiment to test the classical elastic nonlinearity of a medium should aim to characterize the elastic nonlinearity coefficient(s) which scale the nonlinear term(s) of the wave equation; in this case, the coefficient β in equation (1.13). Here we simplify this process by using an indirect measure of a material's classical elastic nonlinearity, namely, a change in wave speed and thus time-of-flight across one of our samples induced by an external strain perturbation (pump wave). We define this indirect indication in equation (1.12); here, V_{S_0} is the wave speed of our sample with no pump transmission and $V_{S_1}(\tau)$ the wave speed with pump transmission (here, τ is the time dependence owing to the time between the transmission of the pump wave and the transmission of the probe wave). Thus, we can derive the material classical elastic nonlinearity by comparing the probe

signal with and without the pump wave's presence.

The experimental design we use, first developed by Gallot et al. (2014) and subsequently by Khajehpour Tadavani et al. (2020) is shown in Figure (2.1). We use an arbitrary waveform generator (Keysight 33500B Series) to excite both the pump and the probe signals. We choose the probe wave to be a low-amplitude (5 V), high-frequency (500 kHz) signal relative to the pump wave's high-amplitude (10 V amplified 50x by a TEGAM HIGH Voltage Amplifier), low-frequency (50 kHz) character. We use a relatively low amplitude for the probe wave to preserve the medium's elastic parameters during the probe's transmission (i.e., the source of perturbation is due exclusively to the pump wave and not the probe). We use a high amplitude for the pump to induce a large enough perturbation to be sensed by the probe wave. We choose the probe and pump frequencies such that the pump wavelength is significantly larger ($\approx x10$) than that of the probe wavelength. This choice results in an approximately steady-state pump wave at the timescale of the probe, thus granting us the ability to sense different phases of the pump waveform with the high-frequency probe.

We choose both the pump and probe to be shear waves (S-waves) which allows for more freedom when defining how we orientate the polarization of the waves relative to different types of inhomogeneities. An S-wave ultrasonic contact transducer with a diameter of 1.27 cm (Olympus PanametricsTM V153) acts as the probe source and an S-wave ultrasonic contact transducer with a 2.54 cm diameter (Olympus Videoscan V1548) as the pump source. We use identical transducers as receivers attached to the opposite face to that of the corresponding source. We couple each of the transducers to a sample using uniaxial squeeze clamps and an ultrasonic coupling agent. We pass the recorded probe signal through a high-pass frequency filter (KROHN-HITE Cooperation Model 3950) with a cut-off frequency of 150 kHz to attenuate any pump

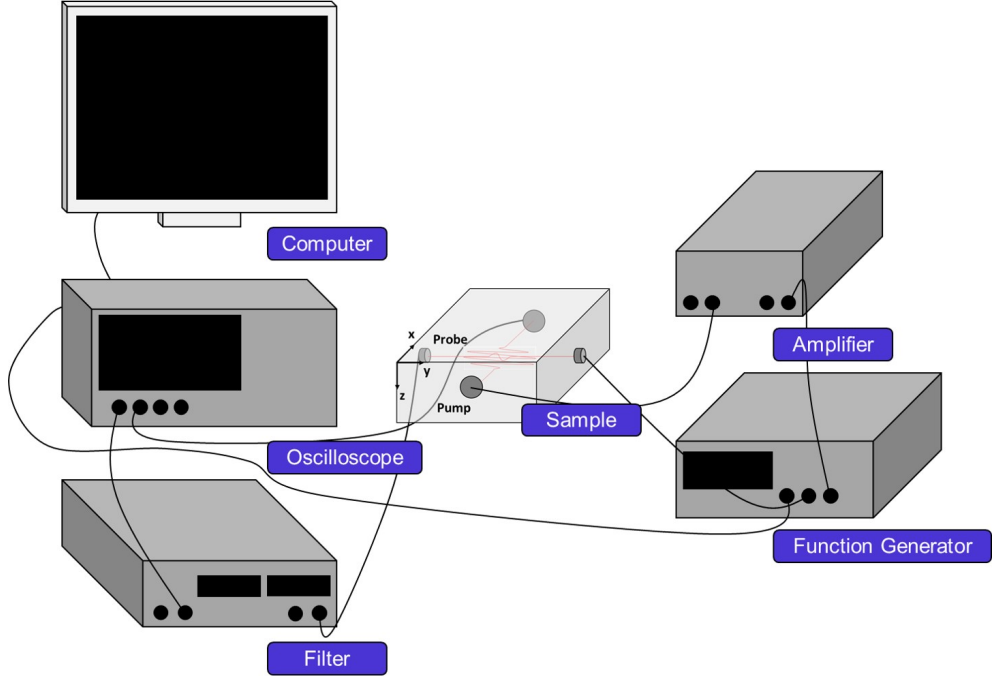


Figure 2.1: The transient wave dynamic acousto-elastic testing (TW-DAET) experimental setup we employ.

signal we measure with the probe receiver. The filtered probe and the pump then feed into a Keysight InfiniiVision MSOX2015a oscilloscope for analysis and recording. The signals recorded on the oscilloscope are then transmitted to a laboratory computer.

The velocity perturbation and thus the probe travel time delay imposed by the pump that we aim to measure is small, on the order of nanoseconds. To measure such a small signal, we adopt the recording workflow developed again by Gallot et al. (2014). The procedure is as follows:

1. Send and record a probe signal, S_1 ,
2. Send and record a pump signal, S_2 ,
3. Send and record a pump and probe signal simultaneously as S_3 ,
4. Calculate the perturbed probe: $S_4 = S_3 - S_2$,
5. Calculate the cross-correlation between the probe signal, S_1 , and the perturbed

probe, S_4 , using

$$(S_4 \star S_1)(\tau) = \int_0^\infty S_1(t)S_4(t + \tau)dt. \quad (2.1)$$

6. Calculate a parabolic fit using the four points nearest the maximum of the cross-correlation function.
7. Take the peak of parabolic fit as the time delay between the probe and perturbed probe.

We repeat this process multiple times at different pump transmission delays to evaluate how the elastic nonlinearity changes with varying phases of the pump. In figure (2.2), we show a schematic view of one of our samples as we progress through three transmission delay values. At $0 \mu s$, the probe interacts with the pump at a minimum, while at $10 \mu s$, the pump wave has progressed such that the probe senses a maximum. Therefore, as we delay transmission, the probe senses multiple transitions between the pump wave's positive and negative polarities, allowing for a complete characterization of elastic nonlinearity. We layout the steps of the data collection process in figure (2.3).

Since we aim to examine the dependence the results of our experiments have on the orientation of internal micro-fractures or embedded inhomogeneities, we define two constant transducer orientations that we will use to compare throughout the project. We define these two orientations in such a way as to maximize the amount of nonlinearity we induce. For the most part, this involves setting up the pump wave such that its polarization is perpendicular to the inhomogeneity in question (we discuss this in more detail in section 4.2.1).

Orientation one, shown in figure (2.4 left), defines the propagation direction of the probe parallel to the y-direction with particle motion parallel to the x-direction. The pump propagates in the x-direction with its particle motion parallel to the y-direction. Thus, the pump and probe waves are contained with the same (xy-) plane

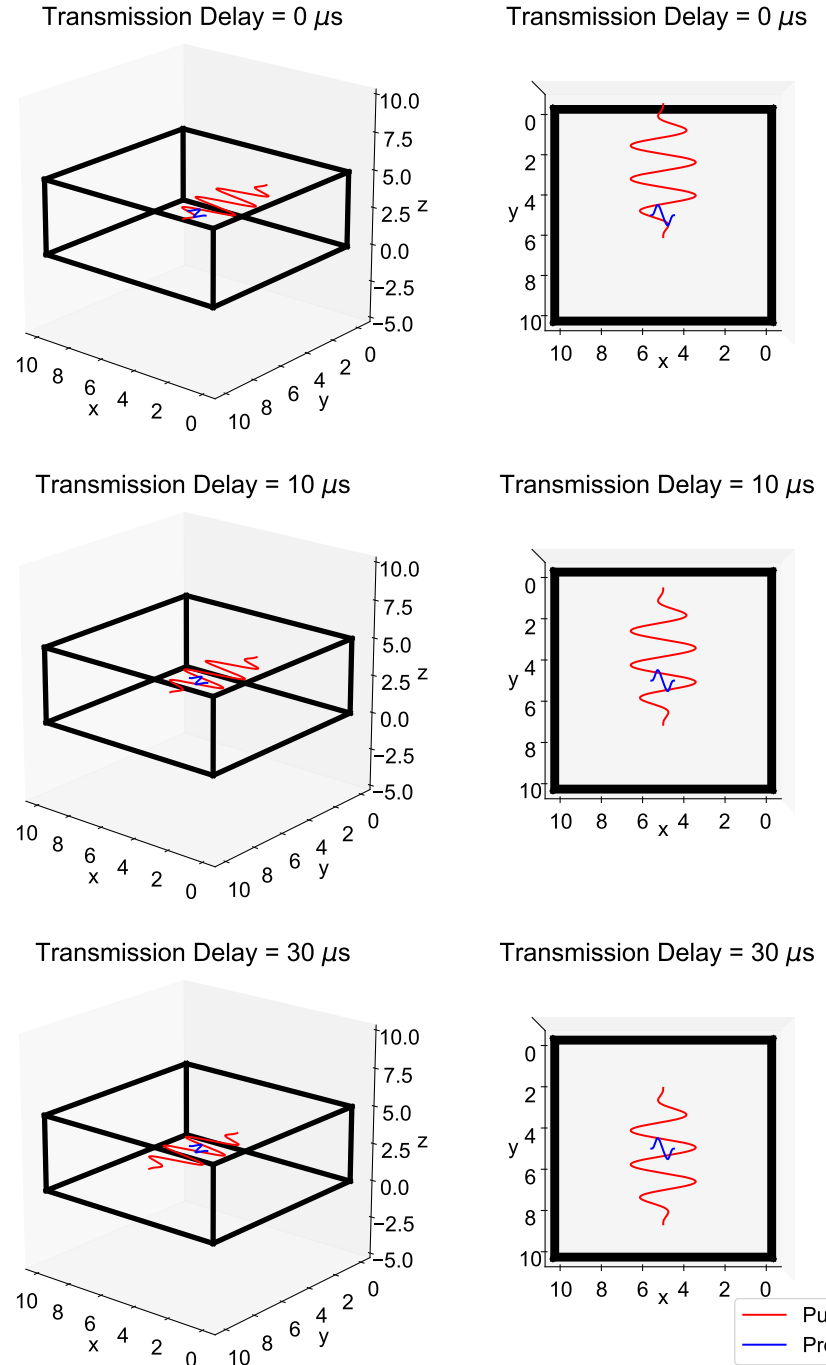


Figure 2.2: We show three transmission delays to depict how the probe (blue) interacts with different pump (red) phases in our samples as we change the transmission delay.

though both transducers are not perfectly focused, resulting in side lobes propagating in the adjacent planes. Orientation two, shown in figure (2.4 right), defines the probe

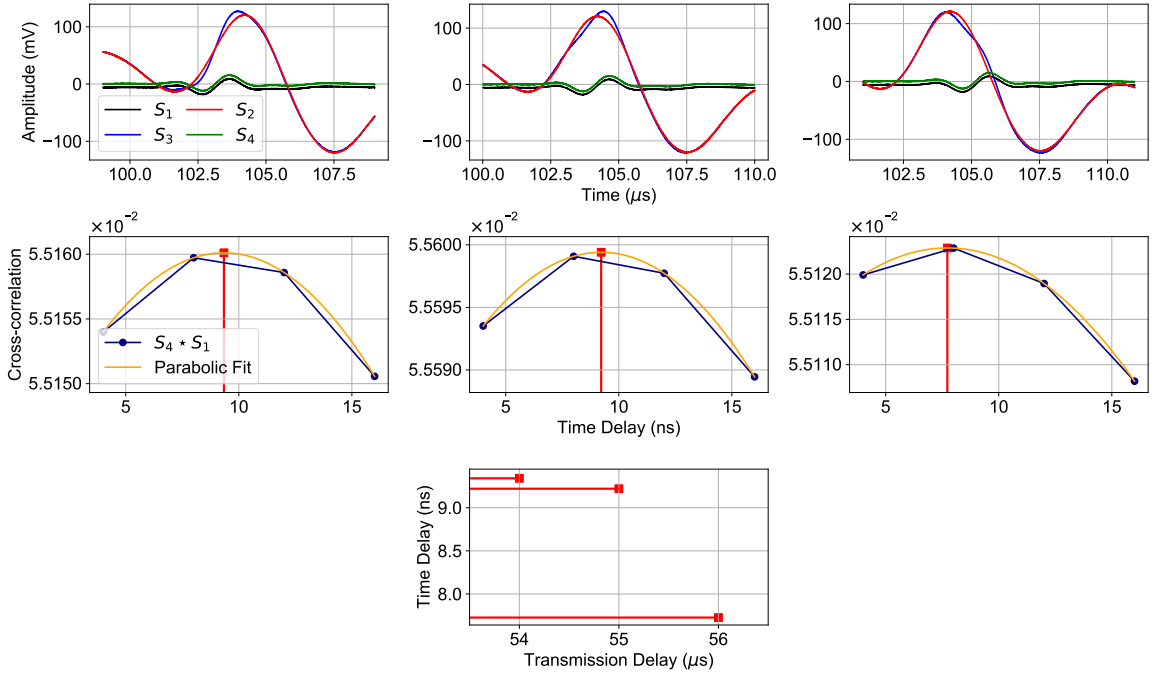


Figure 2.3: Shown here is the probe time delay calculation process for three transmission delays. Row one shows the recorded waveforms ($S_{1,2,3}$) and the calculated perturbed probe (S_4). Row two shows the cross-correlation function along with the parabolic fit for the unperturbed and perturbed probe signals (i.e., $S_4 * S_1$). Note that the parabolic fit maximum (red square) corresponds to the probe time delay at that particular transmission delay (plotted on the y-axis in row three).

to propagate in the z-direction with its polarization parallel to the x-direction. The pump's propagation direction is left constant in orientation two, but we rotate the transducers 90 degrees such that the polarization is now parallel to the z-direction. Again, as in orientation one, the pump and probe waves are contained within a single (xz-) plane.

Figure (2.5) shows the results of a preliminary scan on a sandstone sample. An inherent time delay difference exists between the two orientations; this is consistent with further experiments and literature review (Haupert et al. (2014)) and is likely due to two main factors. One of these factors is elastic nonlinearity anisotropy because of a non-random distribution of inherent micro-defects (grain-to-grain boundaries, micro-fractures, etc.) within the medium. The second factor contributing to this difference is the perpendicular polarizations of the pump and probe waves. It is well established

that the non-linear effect is more prominent when the polarizations of these two waves are parallel (Hamilton et al. (2008)). Since we compare all of our experimental results to a baseline, unperturbed set of time delays, we can easily account for any inherent orientation difference that may exist.

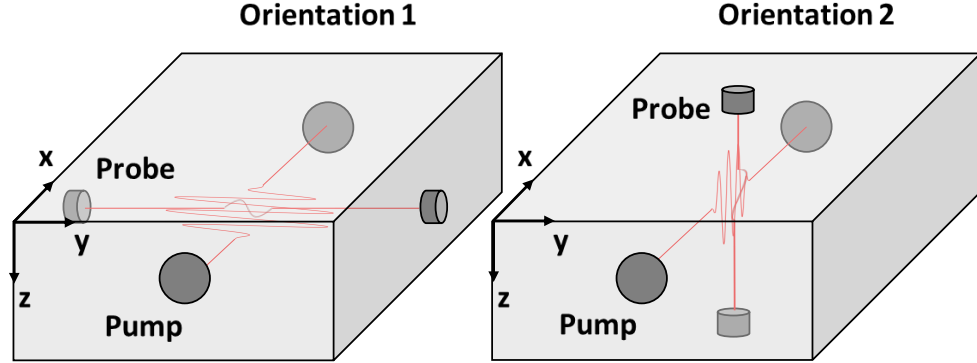


Figure 2.4: Here we show the pump-probe orientation diagrams employed during TW-DAET. Orientation one (left) defines the pump and probe propagation directions parallel to x and y, respectively, with each wave, polarized vice-versa. Orientation two (right) defines propagation directions of the pump and probe in x and z, respectively, again with each wave polarized vice-versa.

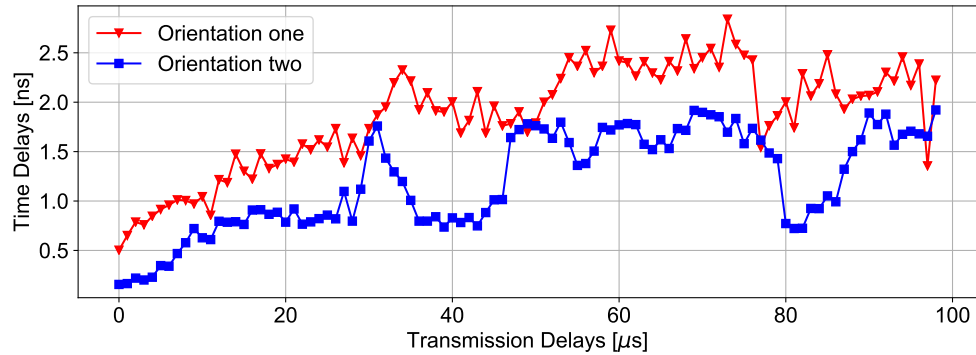


Figure 2.5: Preliminary time delay results from a sandstone sample. Note the inherent difference seen between orientation one (red) and orientation two (blue).

2.2 Fracturing Work Flow

In the following section, we lay out the project's two main branches of sample creation. The aim of the first branch (section 2.2.1) is to induce a known micro-fracture network into sandstone samples using forces of expansion. We aim to align this network by defining a maximum principal stress axis in the sample while inducing expansion. We saturate samples with two liquids: tap water and salt-saturated water to increase expansion via freezing with the former and freezing plus salt precipitation with the latter. The second branch (section 2.2.2) involves creating multiple cement samples with different levels of embedded inhomogeneities. Using this type of sample, we will aim to detect the presence of these inhomogeneities and sense their orientation with our transient wave dynamic acousto-elastic testing (TW-DAET) setup.

2.2.1 Freeze-thaw Fracturing

Tap Water

It is a well-known fact that when water moves from its liquid to solid state (i.e., freezes) it undergoes a volume expansion. This is contrary to most liquids as generally the transition into the solid phase comes with a volume contraction. This expansion rather than contraction is due to the open hexagonal form of the water's crystalline lattice. This increase in volume, about 9% as shown in figure (2.6), can generate significant amounts of stress when the phase transition occurs in a confined space (e.g., pore space). Recent work by Kharseh (2018), shows the utilization of this stress to propel a small go-kart. We aim to utilize this stress to induce micro-damage in our samples caused by the freezing of pore water.

Examples of this type of mechanical damage in rocks can be observed everywhere air temperature falls below 0° C. This damage is in fact a common type of erosion is

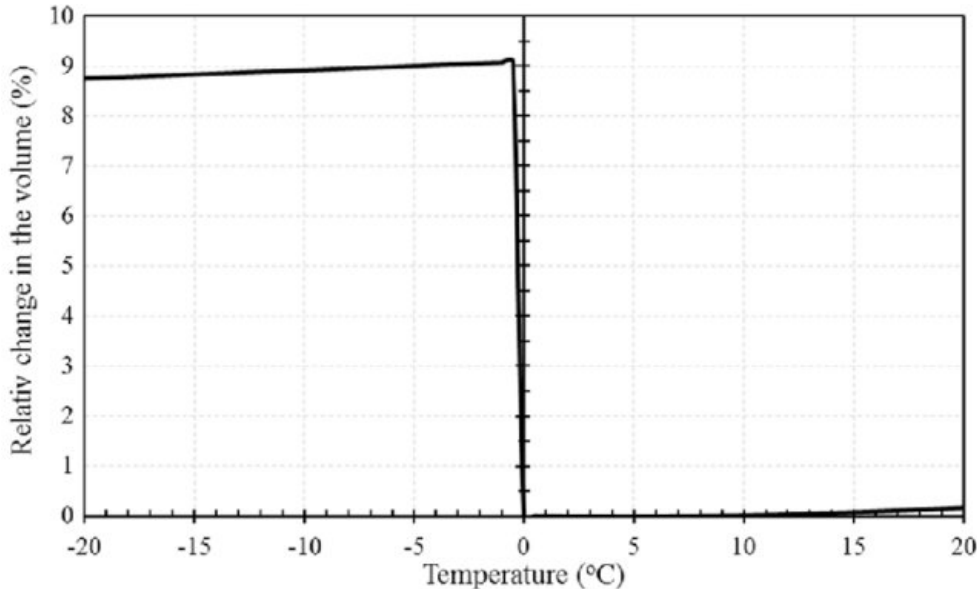


Figure 2.6: Relative change in water volume (%) as external temperature progresses through its freezing point of 0° C. From Kharseh (2018) used under the terms of the Creative Commons Attribution 4.0 International License (<http://creativecommons.org/licenses/by/4.0/>).

arctic regions. The slight complication that befalls us with this work, is controlling the direction of the fracture propagation. We attempt to overcome this hurdle by defining a maximum principal stress axis during the freezing process. Fractures tend to propagate in the direction of maximum principal stress and therefore by defining this axis within our sample during the freezing process, any strain induced by the volume expansion of the pore water should culminate in micro-fractures aligned with the maximum principal stress axis. We induce this axis via a uniaxial mechanical vise shown on one the sandstone samples in figure (2.8).

We start this process with six sandstone samples acquired from a quarry in Nova Scotia, Canada. The samples first must be saturated in water; we achieve this by submerging each sample individually within a vacuum chamber which is subsequently pressured to 100 kPa for a 24 hr time period. The samples are then placed in a freezer at $-20^{\circ} \text{ C} \pm 2^{\circ} \text{ C}$ for 24 hours, attaching the uniaxial vise to define the maximum principal stress axis. Finally, we place the samples in an oven at $80^{\circ} \text{ C} \pm 5^{\circ} \text{ C}$

for another 24-hour period to extract any impregnated water. Figure (2.7) shows the sample weights during each phase (initial, saturated and dried) of the workflow. Note that we remove approximately 8 g of water, on average, more than we add. This additional water stems from moisture content present before saturation. We complete

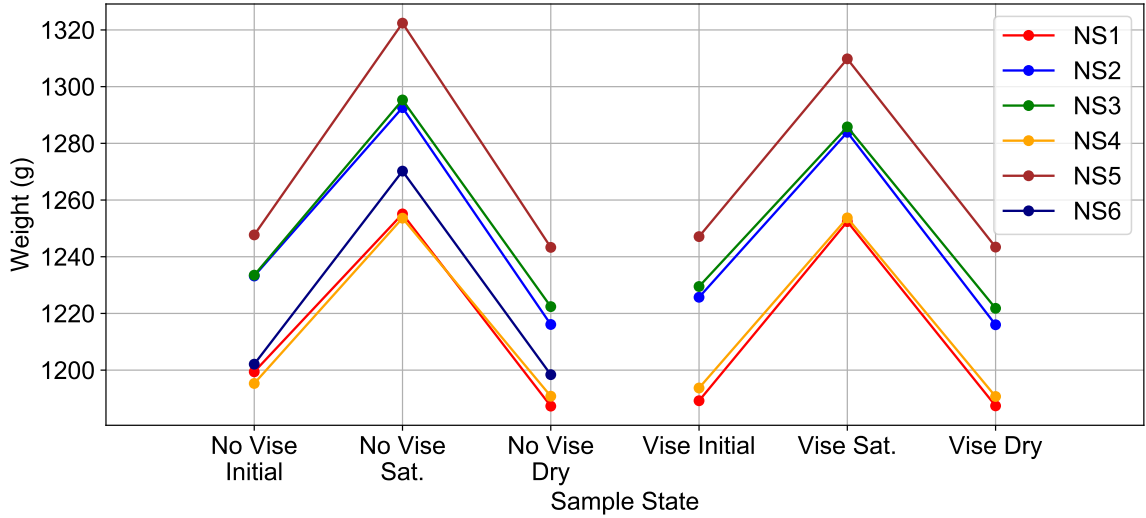


Figure 2.7: Weights of six sandstone samples (NS1-6) at each stage of the tap water freeze-thaw process with and without the vise (note that we detached the vise during the weighing process). The average water weight we add during the saturation process is 61 g, and the average we remove during drying is 69 g.

this process on each of the samples two times; the first, without the vise to collect initial data (i.e., non-fractured), and the second with the vise for the fractured data (figure 2.8).

Salt-saturated Water

To further our attempt to change pore pressure, to be subsequently released via uniaxial strain, we iterate our freeze-thaw fracturing workflow. With this iteration, instead of saturating with tap water, we now use a saltwater solution made up of 15% MgSO₄ and tap water. We also choose one sample (NS5) and complete multiple iterations of saturation, freezing, drying and data collection instead of implementing

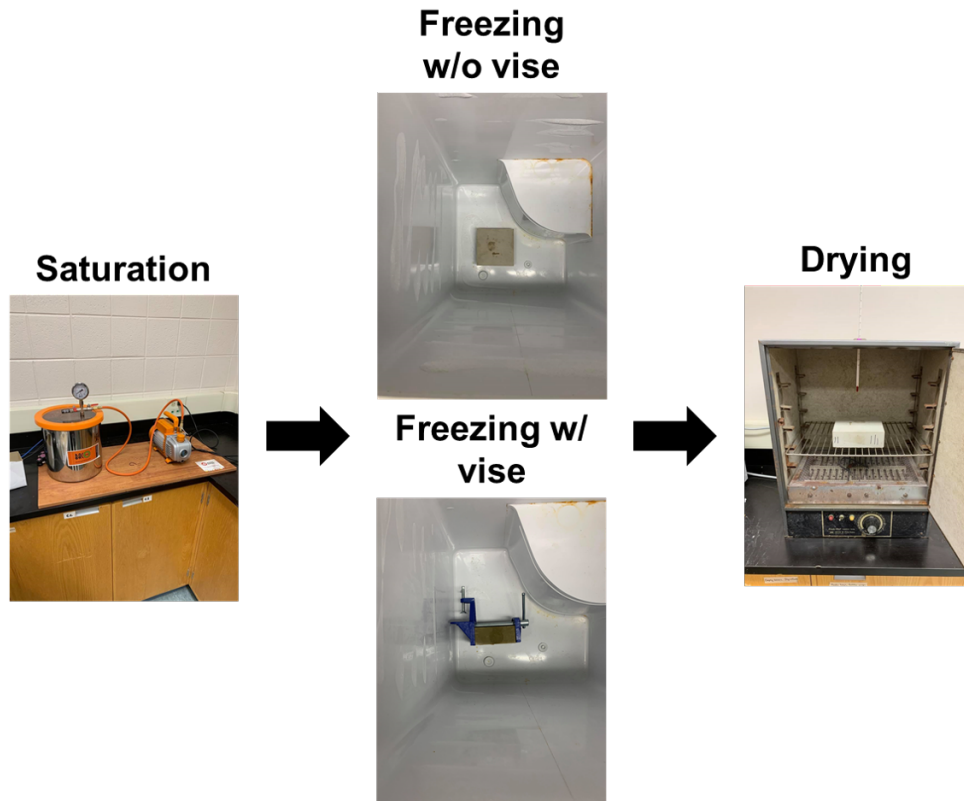


Figure 2.8: Flow diagram depicting the freeze-thaw process: 1. Sample saturation with tap or salt-saturated water in a vacuum chamber; 2. Sample freezing with and without the vise (we complete the entire workflow twice with each sample); 3. Sample drying in an oven.

the process on multiple samples. With the latter difference, we aim to progress micro-damage within the sample initialized during a previous iteration. We complete four iterations, collecting time delay values in both orientations after each.

Using salt-saturated water during the freeze-thaw process, along with a slight temperature increase during the drying stage ($80^\circ \text{ C} \pm 5^\circ \text{ C}$ to $100^\circ \text{ C} \pm 5^\circ \text{ C}$) increases pore pressure due to the expansion of the salt as it precipitates during the drying the process. This expansion is a common type of defect seen in cement infrastructure (i.e., expansive salts damage); Bentahar et al. (2019), use salt-saturated drying to induce damage which they then observe via nonlinear elastic testing (while nonlinear, substantially different than the testing we show here).

With this salt-saturated water variation of the freeze-thaw process, we aim to

induce pore pressure in two ways. First, from the expansive forces of water as it freezes within the confined pore space (freezing stage). Second, the precipitation of salt within the pore causing, again, an expansive force due to its volume increase (drying stage). The uniaxial vise defines the maximum principal stress axis throughout this whole process.

2.2.2 Cement Models

We create multiple synthetic cement models to better constrain the source of elastic nonlinearity we observe through dynamic acousto-elastic testing and therefore better constrain any orientation dependence we find. Seven prismatic, cement samples are investigated; a homogeneous model to act as baseline to compare with other samples and six samples with differing inhomogeneities to explore their effect on elastic nonlinearity. We create all cement samples under equal conditions; equal mix ratios (1:5.5 water-cement ratio), approximately equal length-width dimensions (thickness range between 6-8 cm), equal vibration time and equal curing conditions (24 hours at room temperature and 24 hours at $50^{\circ}\text{C} \pm 5^{\circ}\text{C}$). Consistency when creating the cement models helps us ensure that inherent defects such as randomly orientated micro-fracturing that form during the curing process are minimized for all samples. The size and type of the inhomogeneities are chosen to simulate both geological lin-eations and geotechnical defects. Table (2.1) summarizes properties (dimensions, thickness and separation of inhomogeneities, velocities and average wavelengths) of all samples under investigation.

The six inhomogeneous samples are shown in figure (2.10). We use unconsolidated sand layers to simulate a network of inner-connected pore space within the sample (figure 2.11 left). This geometry somewhat represents that of the Crab Orchard Sandstone, a well characterized sandstone in rock physics research that has aligned

porosity defined by its bedding layers (Benson et al. (2005)). We use a medium- to fine-grain, moderately sorted, subangular to rounded sand made up of approximately 70% quartz, 20% lithic fragments, 5% feldspar and 5% mica (figure 2.9). The first sand sample (2.10 A) consists of three sand layers with an even vertical distribution (separation \approx 1 cm). Each sand layer has equal dimensions of 13 cm x 6 cm x 1 cm. The second sand sample (figure 2.10 B) is kept largely consistent with the first, changing only the thickness of the three layers resulting in the dimensions 13 cm x 6 cm x 0.5 cm. Note that due to the thickness change, the separation between the layers also increases. The dimensions of the sand layers in the third sand sample (figure 2.10 C) remain at 13 cm x 6 cm x 0.5 cm while we decrease the separation between the layers to 0.5 cm. We also increase the number of layers from three to seven. Different thicknesses, both of the unconsolidated sand beds and the interval between the beds, are investigated and are later shown to affect the nonlinear response of the sample.

Three approximately ten-centimeter-long metal rods are used in one sample to simulate the detection of cemented infrastructure with TW-DAET (figure 2.10 D and figure 2.11 middle). Because of the dimensions of these rods, an inherent orientation difference is created within the sample. We will try and observe both the presence of the rods (i.e., the detection scenario) but also the orientation of these rods. We use a network of ten thin copper wires spaced 5 millimeters apart (10 cm x 4.5 cm) lying flat in the xy-plane in the center of the sample to simulate a network of thin, closely spaced lineations (figure 2.10 E and figure 2.11 right). Our final sample also uses a network of copper wires to form the inhomogeneity but this time at a separation of 10 millimeters resulting in the wire network dimensions 10 cm x 9 cm (figure 2.10 F). As with the unconsolidated sand samples, we choose to employ cylindrical, metal inhomogeneities of varying diameter and varying separation to explore how these

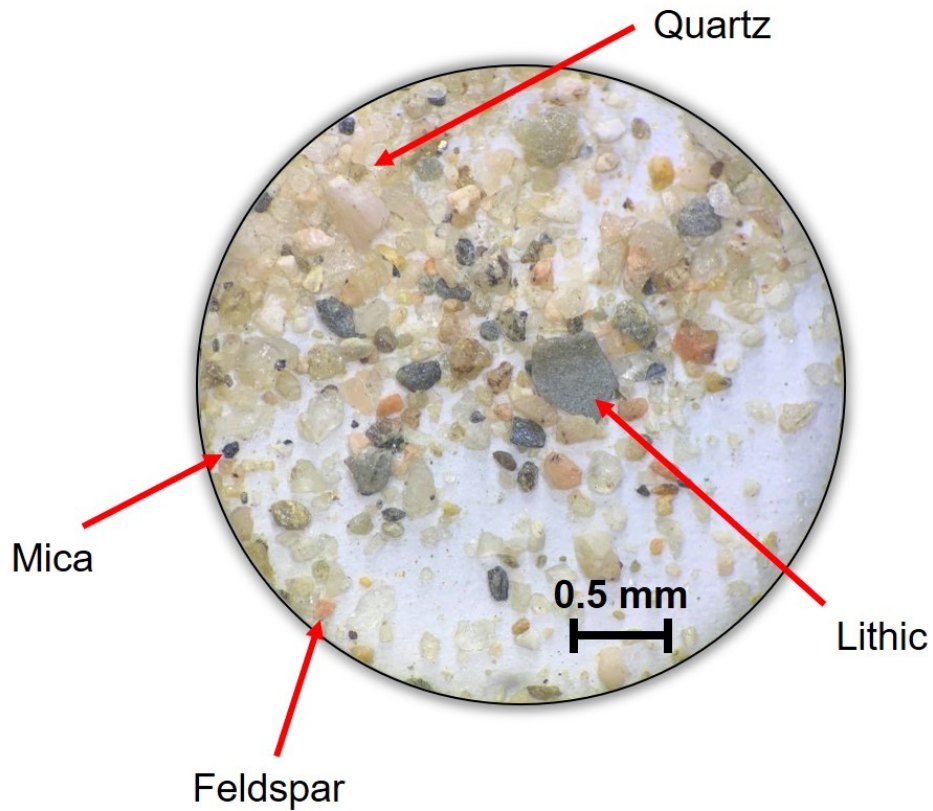


Figure 2.9: Magnified image of the sand we use to create samples CS1-3.

differences may change the elastic nonlinear response. Specifically, we attempt to develop a connection between the response from our TW-DAET experiment and the relationship of the probe wavelength to inhomogeneity separation and thickness. We discuss this connection further in chapter (4).

Table 2.1: Table summarizing the properties of all samples under investigation. Homogeneous cement (CH), cement with sand (CS), cement with metal rods (CR), cement with copper wires (CC) and Nova Scotian sandstone (NS). Properties include: the length (l), width (w) and height (h) of each sample; thickness (t) and separation (s) of inhomogeneities; Pump (pu) and probe (pr) shear velocity (V_s) in all directions (x, y, z); Wavelength (λ).

Sample Units	x mm	y mm	z mm	t mm	s mm	v_{sxpr} m/s	v_{sypr} m/s	v_{szpr} m/s	v_{sxp} m/s	v_{sy} m/s	v_{sz} m/s	λ_{pr} mm	λ_{pu} mm
CH1	183	117	51.8	N/A	N/A	1820	1920	1790	1830	1870	1730	3.69	36.1
CS1	183	115	47.7	10.0	≈ 5	1720	1800	1650	1820	1770	1590	3.44	34.5
CS2	181	114	35.5	5.00	≈ 5	1780	1910	1810	1780	1870	1780	3.67	36.2
CS3	182	114	47.9	5.00	5.00	1840	1880	1840	1860	1980	1900	3.71	38.3
CR1	182	114	37.6	N/A	≈ 30	2080	1990	1970	1700	1850	1890	4.02	36.2
CC1	182	115	39.9	N/A	5.00	2170	2180	2000	2200	2150	1780	4.24	40.8
CC2	182	115	43.9	N/A	10.0	2050	2130	2170	2070	2020	2090	4.18	41.4
Averages	182.1	114.9	43.47	N/A	N/A	1920	1970	1890	1890	1930	1820	3.85	37.6
SD	0.6	0.1	6	N/A	N/A	200	100	100	200	100	200	0.3	2
NS1	101	103	50.8	N/A	N/A	2080	2050	1960	2010	1950	1888	4.06	38.9
NS2	102	103	51.7	N/A	N/A	2090	2040	1970	1970	2010	2040	4.06	40.1
NS3	103	103	51.9	N/A	N/A	2080	2070	2000	2060	2060	2050	4.10	41.1
NS4	102	102	52.0	N/A	N/A	2060	2070	2010	2000	2040	1990	4.09	40.1
NS5	104	103	51.8	N/A	N/A	2360	2410	2200	2030	2330	2120	4.65	43.2
NS6	101	101	52.6	N/A	N/A	1930	1940	1870	2100	1970	1750	3.82	38.8
Averages	102	103	51.8	N/A	N/A	2100	2100	2000	2020	2060	1970	4.13	40.4
SD	1	0.8	0.5	N/A	N/A	100	200	100	40	100	100	0.3	2

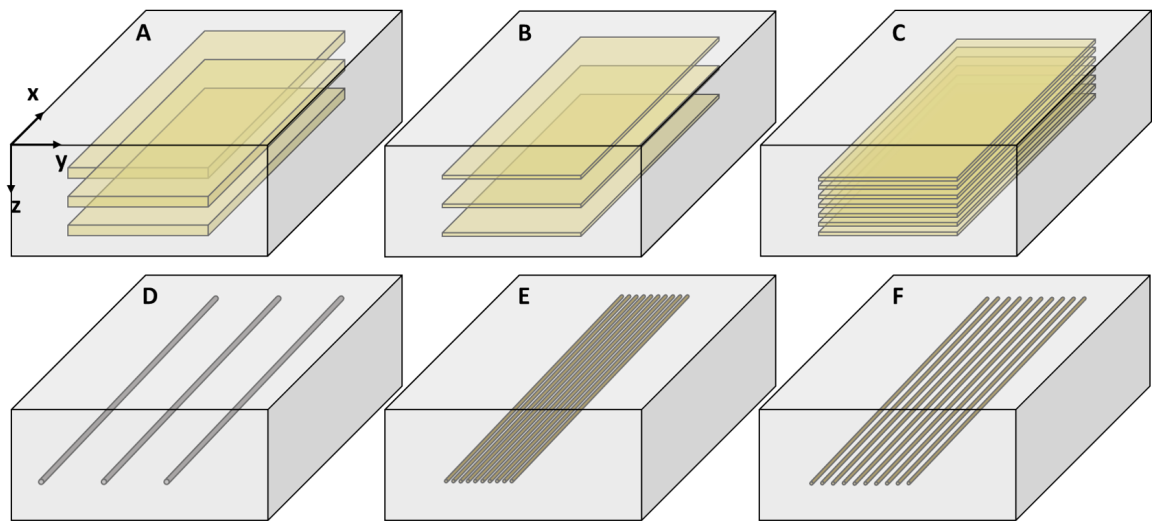


Figure 2.10: Schematic depicting the six prismatic inhomogeneous cement samples on which we complete TW-DAET. Samples A, B, and C consist of embedded unconsolidated sand layers of varying thickness and separation. The inhomogeneities in samples D, E, and F consist of two types of metallic cylinders (metal rods; D and copper wires; E and F) again with varying diameter and separation. Note that schematic diagrams are not to scale.

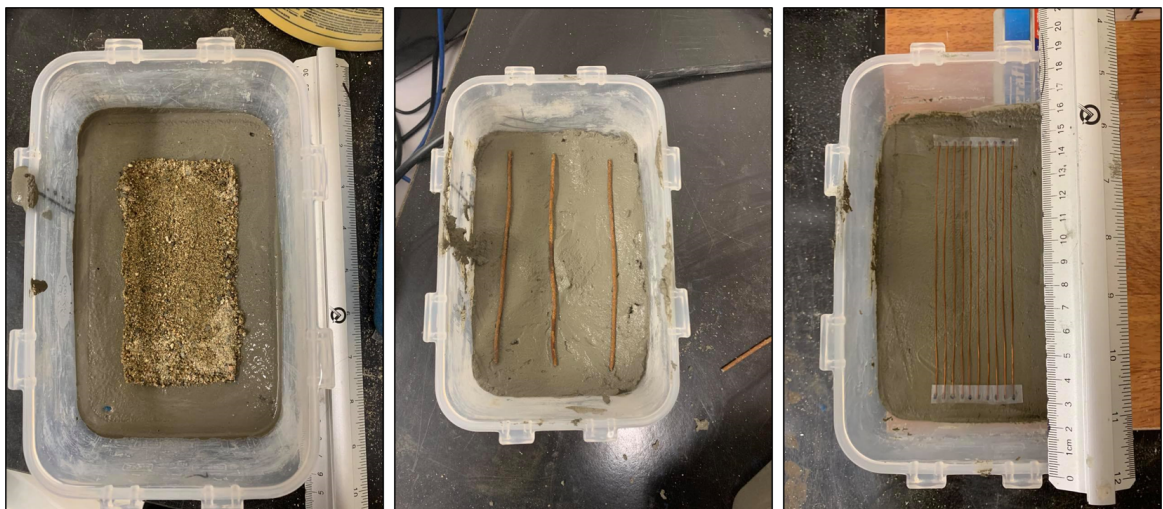


Figure 2.11: Shown are three inhomogeneous cement samples before the addition of the top layer of cement. Left: Thick unconsolidated sand layers; Middle: metal rods; Right: ten copper wires separated by five millimetres.

Chapter 3

Experimental Results

Below we present the project's experimental results; We first show time delay values from sandstone samples which we perturb via freeze-thaw fracturing with tap water (section 3.1.1) and saline water (section 3.1.2). We then go on to present time delay results from cement samples with different levels of embedded inhomogeneity including thick sand layers (section 3.2.2), thin sand layers (sections 3.2.3 and 3.2.4), metal rods (section 3.2.5) and copper wires (sections 3.2.6 and 3.2.7). We compare these inhomogeneous samples to their homogeneous counterpart, which is inherently linear, to further the claim that we can use transient wave-dynamic acousto-elastic testing (TW-DAET) to image the inhomogeneities.

We observe three main components that make up the majority of data we collect, which we define based on their distinct frequencies (figure 3.1). These components, tend to have different amplitudes and rates of attenuation depending on the particular sample we are testing. Considering the consistency of the presence of these components and their variation between different samples, it is useful to define and label their character to aid in the following interpretations and discussions.

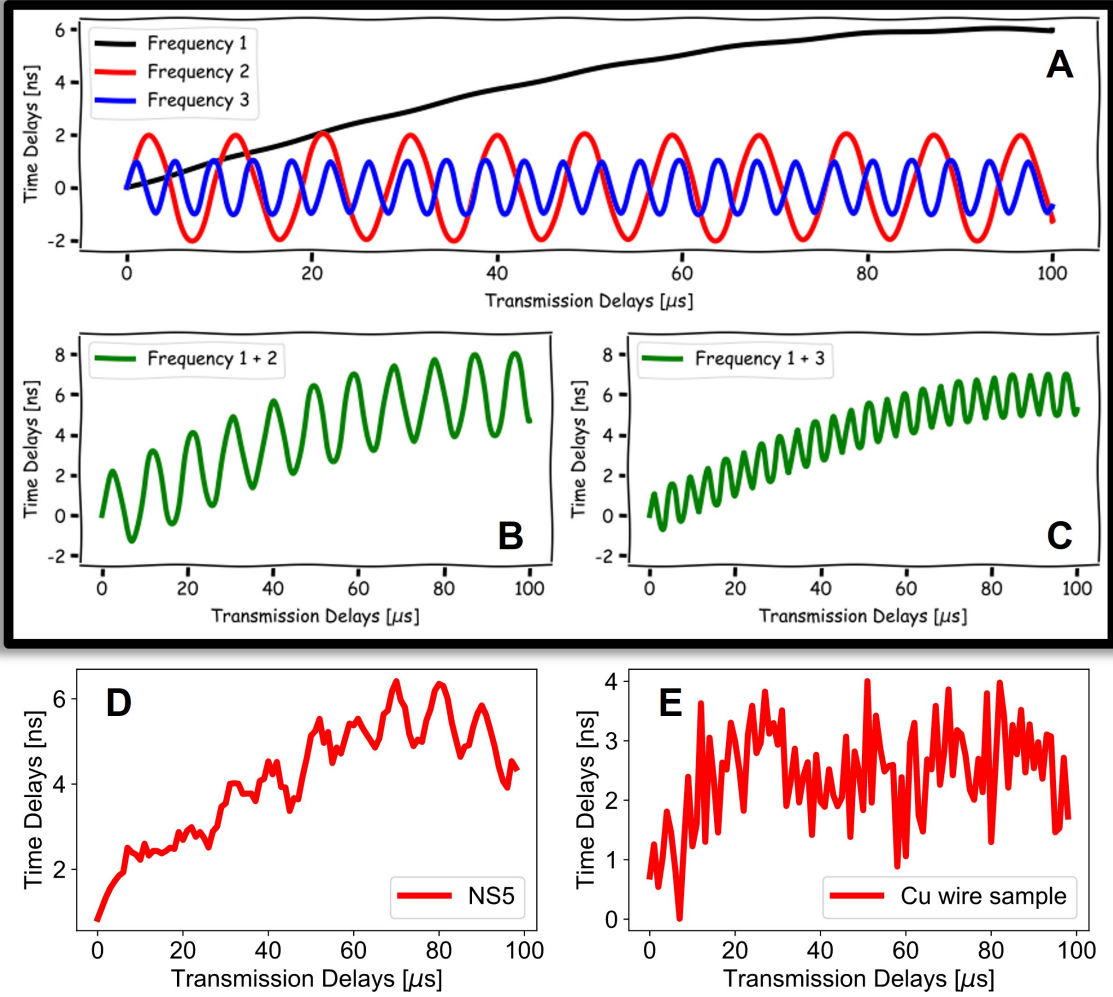


Figure 3.1: A: schematic depicting the three main components of time delays at their distinct frequencies (1, 2 and 3). Schematics depicting the addition of components at frequencies one and two (B) and frequencies one and three (C). Examples of time delays with a clear presence of frequencies one and two (D; NS5) and frequencies one and three (E; CC1).

3.1 Freeze-thaw Fracturing Results

Below, we present the probe time delay plots for the freeze-thaw fracturing workflow.

As discussed in section (2.2.1), we saturate six sandstone samples with tap water and one sandstone sample with 15% MgSO₄ water. The tap water samples are then kept at $-20^{\circ}\text{C} \pm 2^{\circ}\text{C}$ for 24 hours with applied uniaxial stress, after which most of the water is removed by drying the samples in an oven. The salt water-saturated

sample is also frozen. Instead of removing the vise and drying at a low temperature, the vise is left during the drying process to align any strain induced during pore salt expansion. Instead of completing the saltwater process on multiple samples, we iterate the process four times on the same model to observe how this evolution changes the elastic nonlinear response of the sandstone.

3.1.1 Tap Water

Given below are the time delay trends before (blue) and after (red) the freeze-thaw workflow for three of the tap water-saturated sandstones (figures 3.2, 3.3, and 3.4). We omit data from samples 1 and 2 due to drastically low signal-to-noise ratios (S/N), related to issues with the experimental setup. Due to the consistency of samples 3, 4, and 5, the data collection of sample 6 was left incomplete.

We observe little change in the time delay responses for three of the sandstone samples. Orientation one, in particular, has remarkable consistency in both the amplitude and frequency character of the signal, considering the process to which samples were subject. This consistency has even gone so far as to redefine the noise level for this experimental setup (previously thought to be approximately ± 1 ns time delay). We discuss this redefinition more in chapter (4). We see a slight reduction of the high-frequency component of the signals in orientation two though the exact physical cause of this result should be interpreted with caution.

Overall, the only time delay differences observed after the freeze-thaw workflow are minuscule. This diminutive change is negligible considering the noise level of our experiments. This negligibility says one of two things about the freeze-thaw workflow: either there is little to no introduction of micro-damage within the samples or, our TW-DAET is not sensitive enough to observe any induced micro-damage. Considering previous work (e.g., TenCate et al. (2016); Rusmanugroho et al. (2019)), we hold more

confidence in the former conclusion.

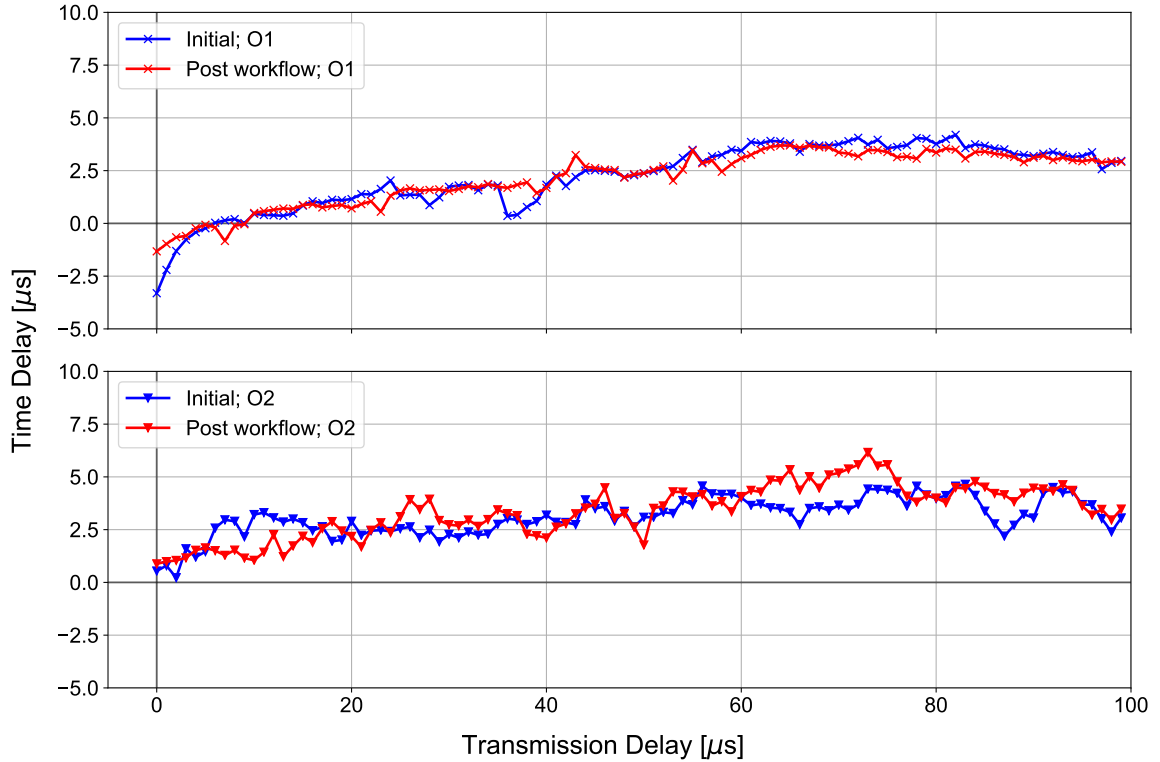


Figure 3.2: Time delay results from sample NS3 orientation one (top) and orientation two (bottom). We compare initial time delays (blue) to the post-freeze workflow time delays (red) for both orientations.

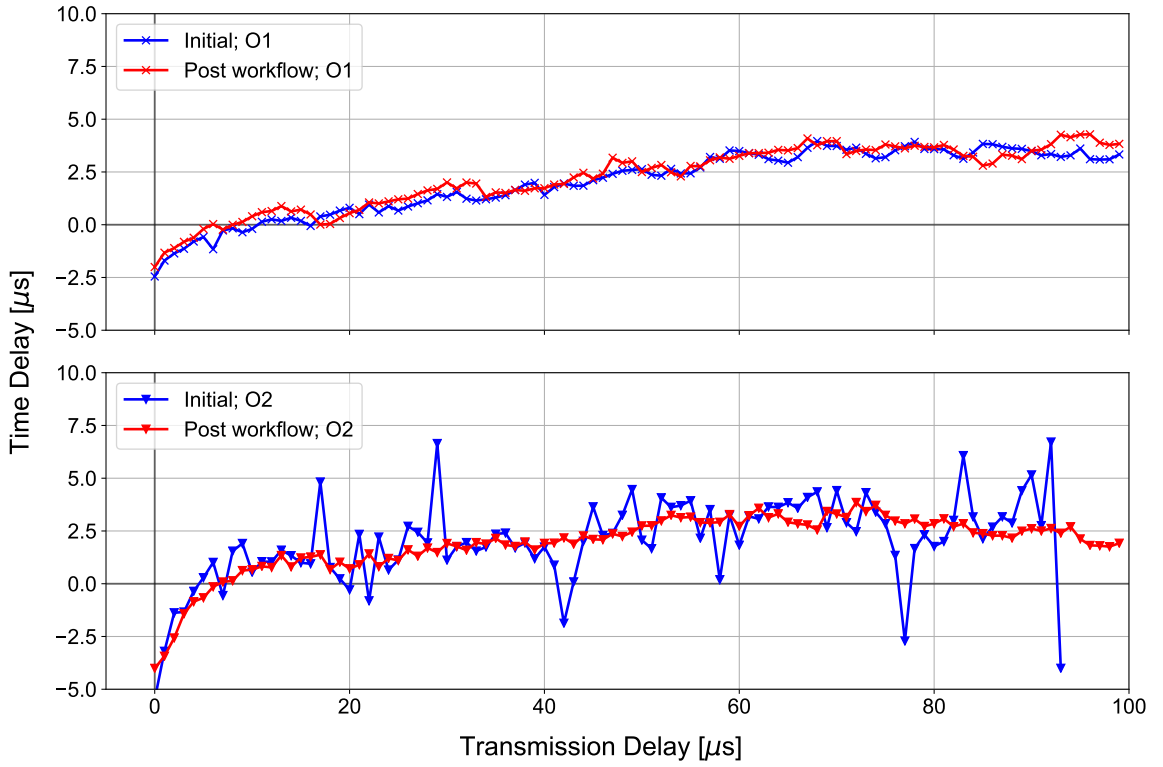


Figure 3.3: Time delay results from sample NS4 orientation one (top) and orientation two (bottom). We compare initial time delays (blue) to the post-freeze workflow time delays (red) for both orientations.

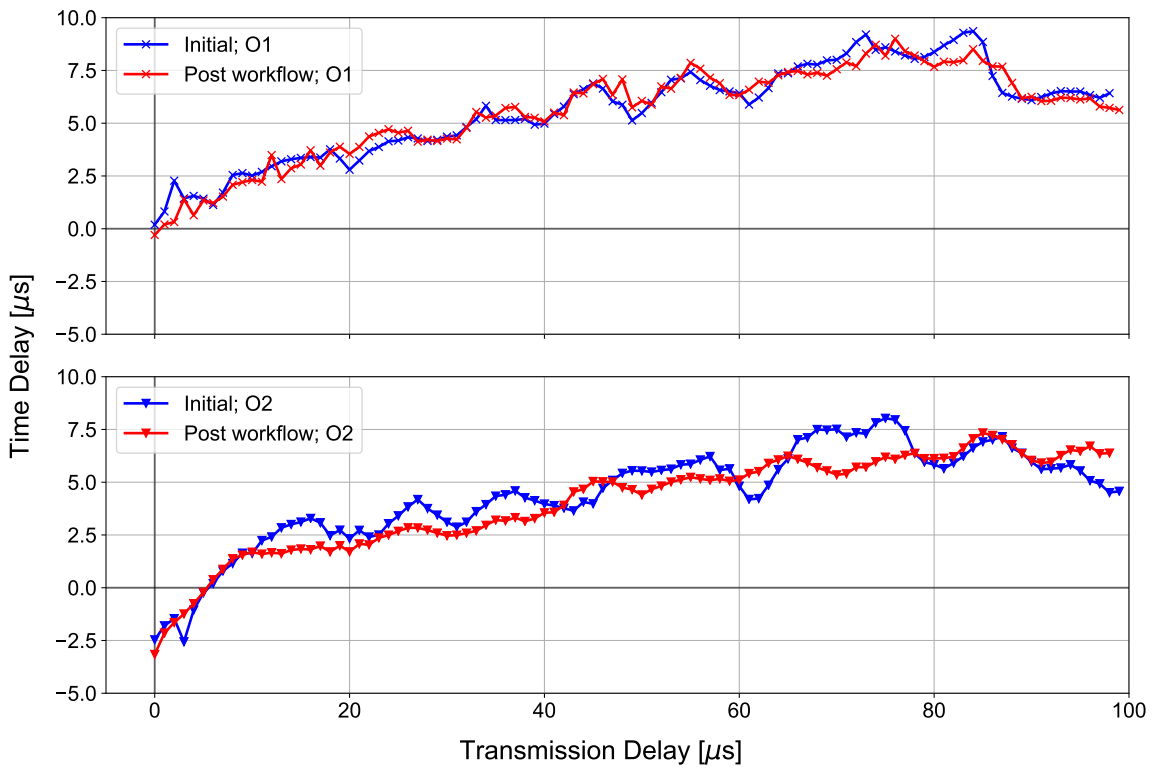


Figure 3.4: Time delay results from sample NS5 orientation one (top) and orientation two (bottom). We compare initial time delays (blue) to the post-freeze workflow time delays (red) for both orientations.

3.1.2 Salt Saturated Water

To generate more expansive stress within a sandstone sample, to be released via uniaxial micro-damage, we saturate one sample with 15% MgSO₄ water and implement the freezing process. We then dry the sample, with the vise, at a higher temperature to increase pore pressure through precipitation of solid salt within the pore space. Note that the salt expansion process is implemented concurrently with the freeze-thaw method, i.e., (1) saturate the sample with saltwater; (2) freeze the sample; (3) heat the sample, all the while with the vise defining the direction of maximum principal stress.

We present the results of the salt-freeze workflow in figure (3.5). We report these results through iterations of saturation, freezing, and drying, of which we have completed four (red trends). We compare these iterations with the initial time delay results (blue trend). Orientations one and two are distinguished by solid and dashed lines, respectively.

The most notable trend we observe from these curves is the overall decrease in time delays, which corresponds to a reduction in elastic nonlinearity as we progress through the iterations. It is important to note that most of the literature points to an increase in elastic nonlinearity with the progress of micro-damage (e.g., Guyer & Johnson (1999)), specifically with micro-fractures in geomaterials (e.g., Xu et al. (2021)). Our results are not consistent with these previous findings. Another marked difference observed from figure (3.5) is the preferential attenuation of the frequency two component in both orientations relative to frequency one (again, note that the frequency components are in reference to figure 3.1). While consistent with a subset of the time delay results from the tap water saturation data, interpretation of this observation should still be made with caution as the frequency content, specifically, the higher frequency components, are quite sensitive to experimental noise.

The one exception to the overall decreasing time delays with increasing iterations comes with the orientation one data for iteration three (figure 3.6). Overall, there seems to exist a faster diminishment of nonlinearity in orientation two relative to orientation one, highlighted significantly in iteration one where the orientation two time delays average approximately two nanoseconds while orientation one sits at approximately 3x that amount. With iteration two, the orientation difference closes (figure 3.6) as the orientation two data reach the approximately linear limiting case (i.e., ≈ 0 ns), allowing orientation one to decrease to this limit also, thus closing the gap in orientation difference. The exception mentioned above arises with iteration three, where the orientation two time delay values remain at the approximately linear end-member, while the orientation one time delays see a pronounced increase. Iteration four sees the decreasing trend continue in both orientations, essentially resulting in both trends arriving at the linear limiting case.

More than one physical mechanism may be at play considering these observations and their consistencies with the data from the tap water-saturated samples. One mechanism controlling the monotonic decrease (while monotonic in both orientations, the rate of decline is different) in time delays as we progress through the iterations and another mechanism that seemly forestalls this monotonicity at least in one orientation. One explanation for this, which we discuss further in chapter (4), uses the idea of two physical mechanisms for which one causes an overall decrease in time delay values while the other causes an overall increase. These two mechanisms occur concurrently, competing to either shrink or grow the time delays with the dominating mechanisms potentially alternating throughout multiple iterations.

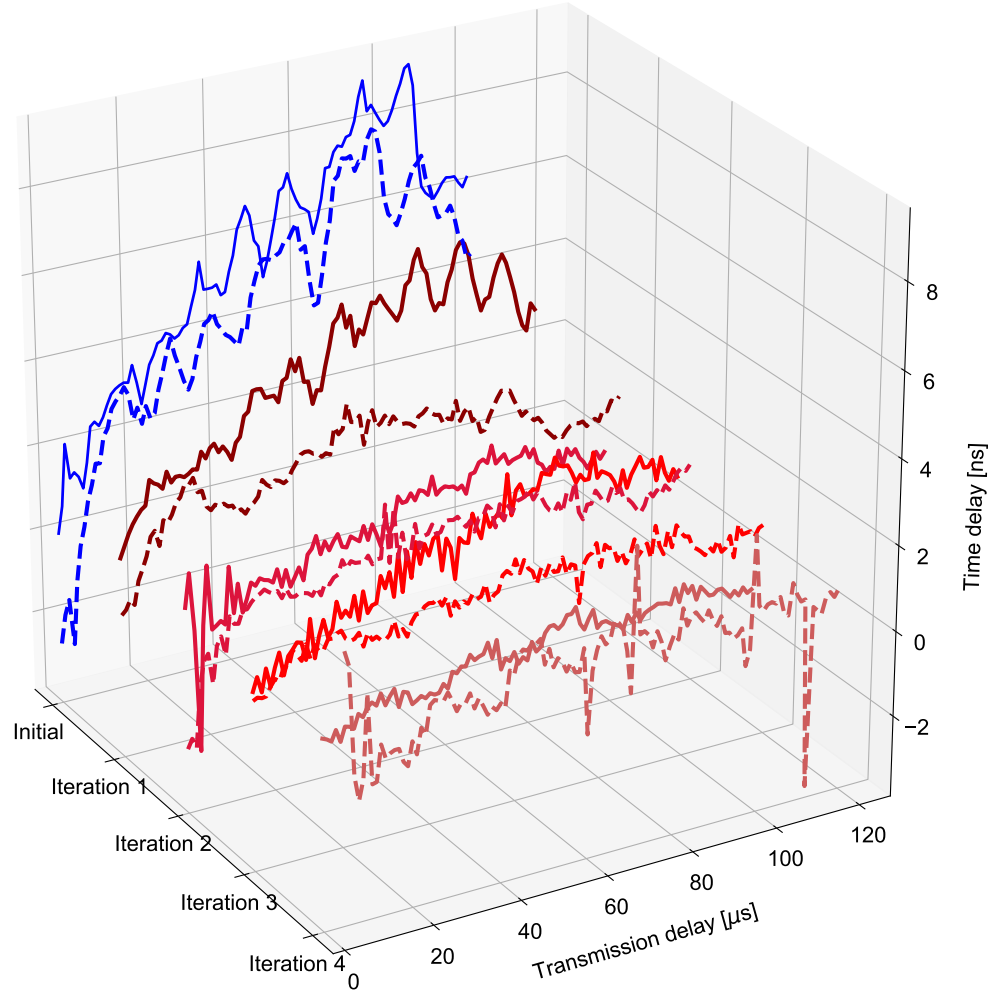


Figure 3.5: 3D projection of the salt-freeze time delay results for the NS5 sample. We show initial time delays (pre-workflow) in the blue solid (orientation one) and dashed (orientation two) lines. Trends in shades of red show progressive iterations of the salt-freeze workflow; orientations follow equivalent line styles.

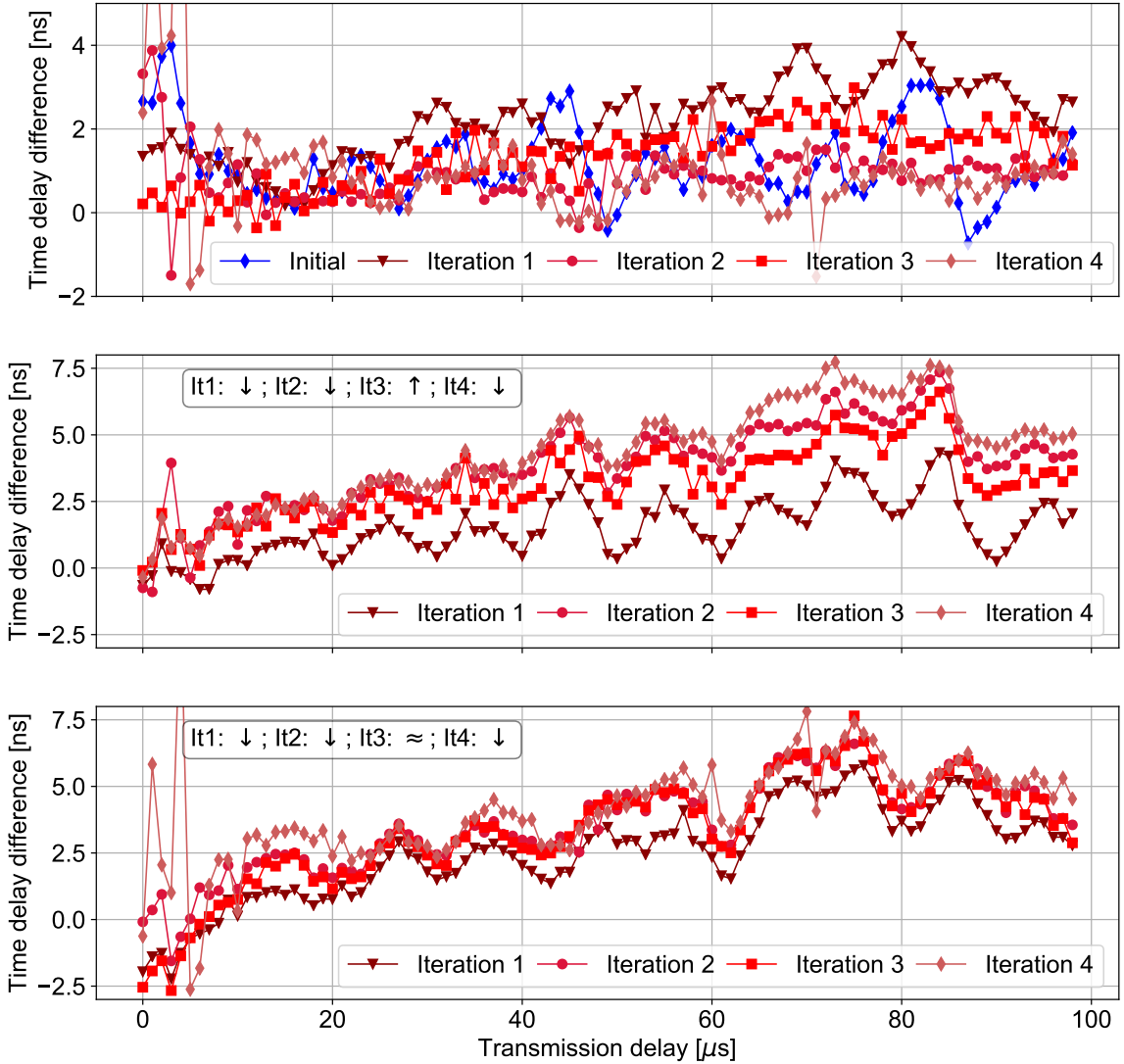


Figure 3.6: Comparison of time delay results for progressive iterations of the salt-freeze workflow. Top: the difference between orientation one and two initially (blue) and through iterations one, two and three (shades of red). Middle: the difference between initial orientation one and iterations one, two, and three orientation one time delays. Bottom: the difference between initial orientation two and iterations one, two, and three orientation two time delays.

3.2 Cement Model Results

In an attempt to control the highly variable nature of samples when using natural geomaterials, such as sandstone, we make a move to control the degrees of freedom by

transitioning into the realm of non-destructive testing. Specifically, we use TW-DAET to scan cement samples with varying degrees of inhomogeneity.

Cement, because of its relatively simple and homogeneous microstructure, is inherently linear. Therefore, by embedding material into cement, we will increase the sample's inhomogeneity, thus increasing the elastic nonlinearity of the material. We work to measure this increase with our TW-DAET experiment by creating six cement samples with different degrees of inhomogeneity (i.e., different embedded materials) and comparing the TW-DAET results from each with the results from a homogeneous cement control sample.

The time delay figures from all the cement samples are presented in the following sections. All figures follow identical formats; The time delay results from the homogeneous control sample are shown in blue, while the results from each particular heterogeneous model are in red. We collect multiple runs on each sample in both orientations to estimate the degree of error that the experiment involves. We distinguish these separate runs with different symbols. Finally, the shaded area shown depicts $\bar{x} \pm 2SD$ where \bar{x} is the mean (dashed line) of each transmission delay, and SD is the corresponding standard deviation. Table (3.1) summarizes the average standard deviations from each of the samples.

3.2.1 Homogeneous Cement (CH1)

As we state above, homogeneous cement is relatively linear compared to materials with higher degrees of complexity within their microstructure. While inherent defects such as small amounts of randomly orientated micro-damage may exist, we follow all necessary mitigating procedures during sample creation to limit this possibility (section 2.2.2). To demonstrate this linearity, we compare the time delay values of aluminum, homogeneous cement and one of the sandstone samples we use in the pre-

Table 3.1: The average experimental time delay standard deviation for each synthetic sample in both orientations. Note the consistently reduced standard deviation in orientation two likely due to the shorter path distance.

Sample	Orientation	Average SD	Number of Runs
CH1	O1	0.43	4
CH1	O2	0.045	4
CS1	O1	0.42	3
CS1	O2	0.16	4
CS2	O1	0.19	3
CS2	O2	0.11	4
CS3	O1	0.55	5
CS3	O2	0.39	3
CR1	O1	1.1	3
CR1	O2	0.87	4
CC1	O1	0.44	4
CC1	O2	0.055	4
CC2	O1	0.52	5
CC2	O2	0.28	5

ceding sections (unperturbed) in figure (3.7). Here we see that aluminum (black), a material with a highly homogeneous structure both macroscopically and microscopically, exhibits virtually no time delay response. Cement (red) is also quite linear, manifesting only minor, high-frequency variations likely due to inherent complexities such as grain-grain boundaries and micro-cracks. Conversely, sandstone (blue) gives rise to time delay values up to 9x higher than that of the aluminum or cement following the inherent elastic nonlinearity of geomaterials.

We show the time delay results from the homogeneous cement for both orientations one and two in figures (3.8) and (3.9), respectively. To evaluate both the level of experimental variation we expect going forward and the amount of inherent nonlinearity in the homogeneous cement, we collect four runs in both orientations.

We note that most of the signal comprises high-frequency oscillation about the 0 ns time delay line, as expected. We also note the decreased S/N of orientation one in comparison to orientation two. We also expect this decrease as the path length for the

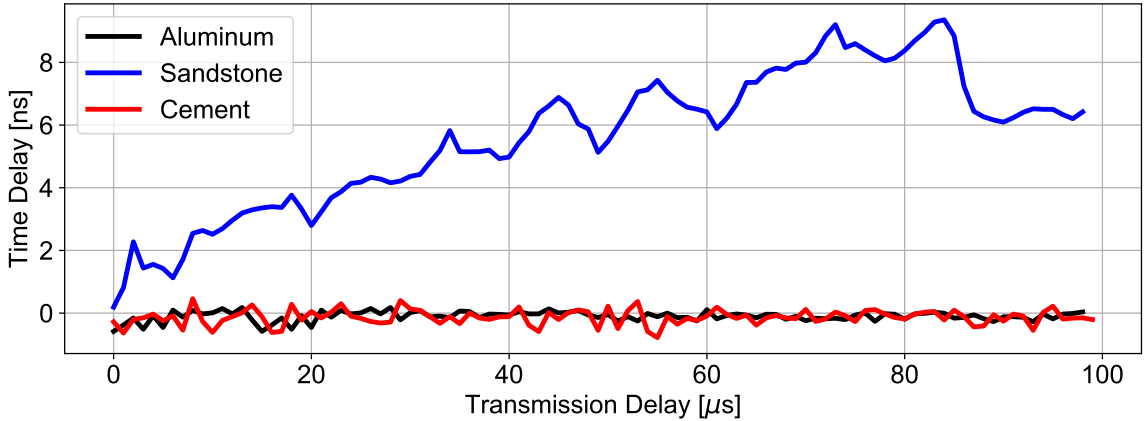


Figure 3.7: Time delay comparison of three materials. Aluminum (black) and cement (red), two inherently linear materials and sandstone (blue), a material with increased elastic nonlinearity.

probe is longer in orientation one and is therefore subject to higher amounts of linear attenuation and thus increased noise sensitivity. This noise anisotropy is consistent across all synthetic samples.

With this result, we define a baseline time delay response in both orientations, which we will use to compare with cement samples with higher degrees of internal complexity. Thus, the goal will be to use time delay responses to identify the presence of heterogeneities within a cement background. As a secondary goal, we also evaluate any orientation dependence these time delays hold based on the spatial character of the heterogeneities. If this connection can be established, the claim that our TW-DAET experiment can be used to image the structure of geomaterials will begin to bear scrutiny.

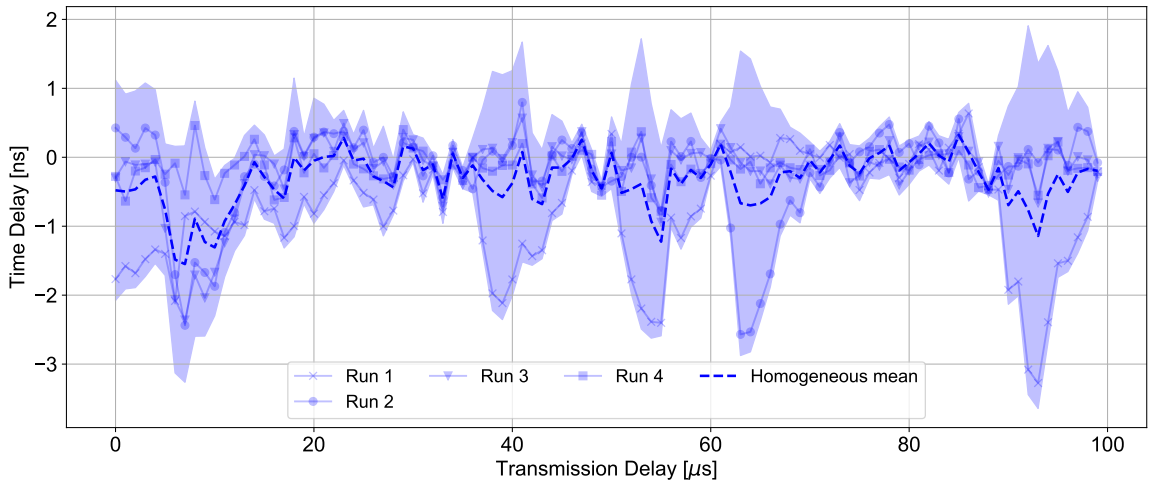


Figure 3.8: Time delay results for the homogeneous cement sample in orientation one. The average trend of four runs is shown (dashed line) with ± 2 standard deviations highlighted by the shaded region.

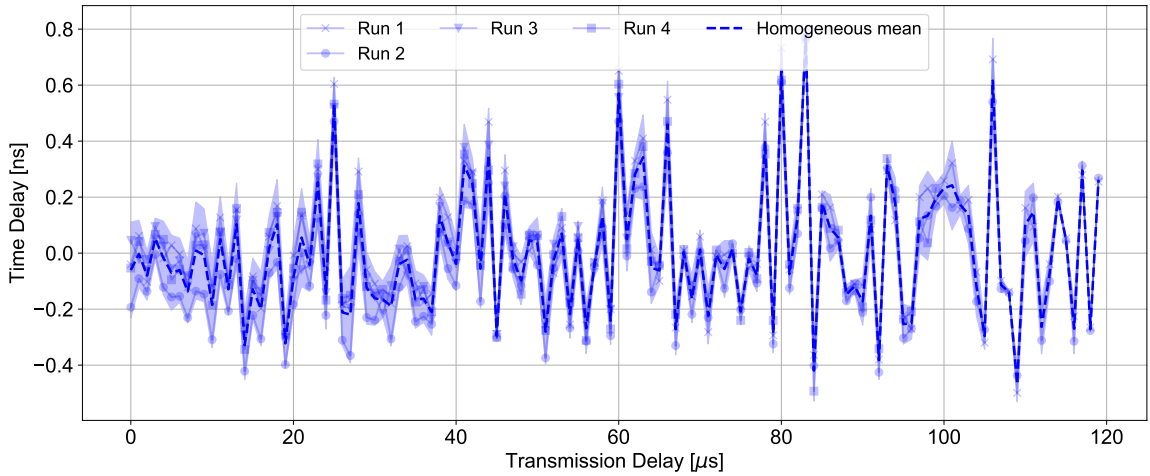


Figure 3.9: Time delay results for the homogeneous cement sample in orientation two. The average trend of four runs is shown (dashed line) with ± 2 standard deviations highlighted by the shaded region.

3.2.2 Cement with Thick Sand (CS1)

We show the time delay results from the cement sample with three one-centimeter-thick layers of unconsolidated sand for both orientations one and two in figures (3.10) and (3.11), respectively. Though the increase in S/N is evident in both orientations relative to the homogeneous time delays, it is quite pronounced in orientation one. Nonetheless, the data is still useful and shows quite consistently little change in time delays, and thus nonlinearity, in both orientations compared with the baseline homogeneous cement results. Recasting this observation in an imaging sense, our TW-DAET experiment fails to observe the presence of the embedded sand layers through the indirect measure of nonlinearity. We attempt to explain this observation using a heterogeneity thickness/probe wavelength dependency discussed in more detail in chapter (4).

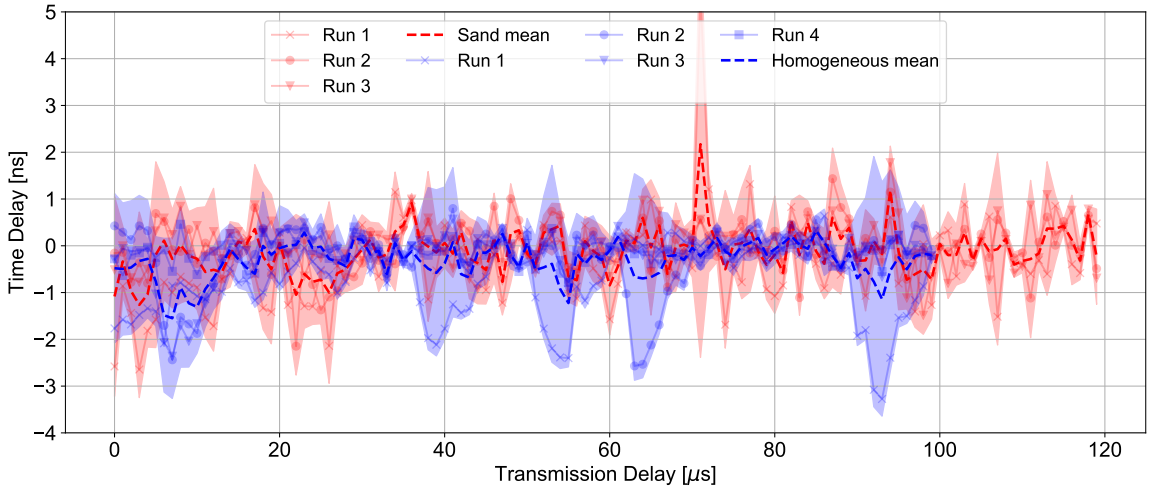


Figure 3.10: Orientation one time delay results for the cement sample with three thick sand layers (red) compared with the homogeneous cement time delays (blue). The average trend of three runs (four runs) is shown (dashed line) with ± 2 standard deviations highlighted by the shaded region.

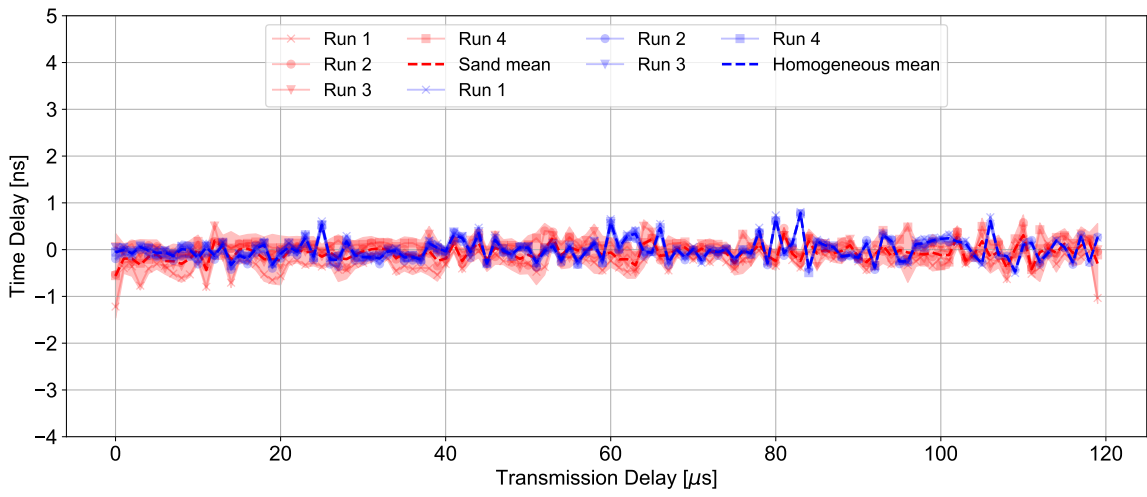


Figure 3.11: Orientation two time delay results for the cement sample with three thick sand layers (red) compared with the homogeneous cement time delays (blue). The average trend of four runs is shown (dashed line) with ± 2 standard deviations highlighted by the shaded region.

3.2.3 Cement with Thin Sand 1 (CS2)

To explore the potential thickness dependence, we use now three thin sand layers ($5\text{ mm} \approx \lambda_{pr}$) with an even vertical distribution, the results of which are shown in figures (3.12) and (3.13).

Following the same convention as above, we observe a small, consistent (low-SD) increase in time delays in both orientations. This increase exhibits an extremely low frequency, essentially resulting in a DC increase of approximately 0.5 ns. Though small, the repeatability of this increase makes this result consistent with a change and inconsistent with noise. Except for small frequency differences, we do not see any evidence to suggest an orientation dependency on the sample's nonlinearity. We discuss both expected and observed orientation dependencies further in chapter (4).

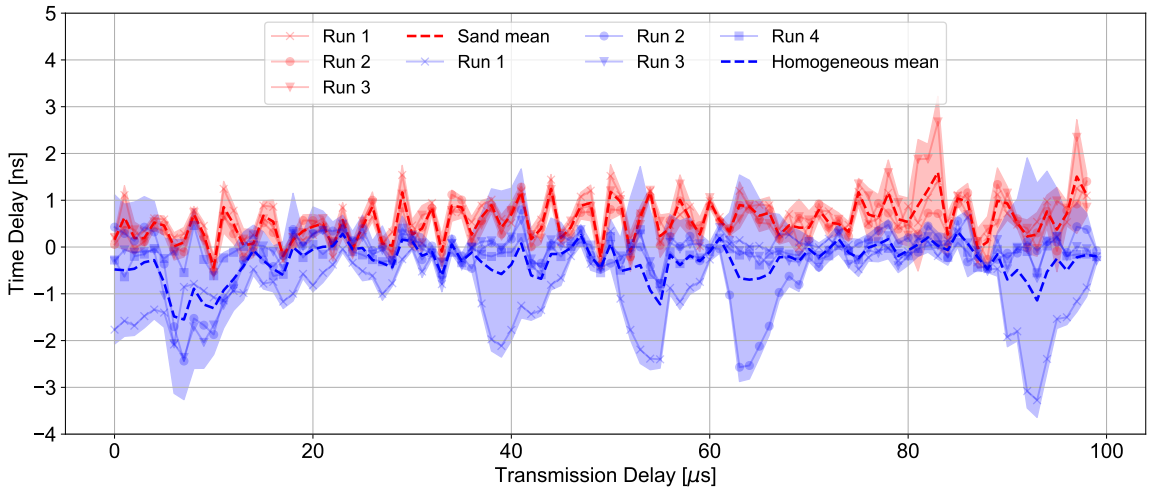


Figure 3.12: Orientation one time delay results for the cement sample with three thin sand layers (red) compared with the homogeneous cement time delays (blue). The average trend of three runs (four runs) is shown (dashed line) with ± 2 standard deviations highlighted by the shaded region.

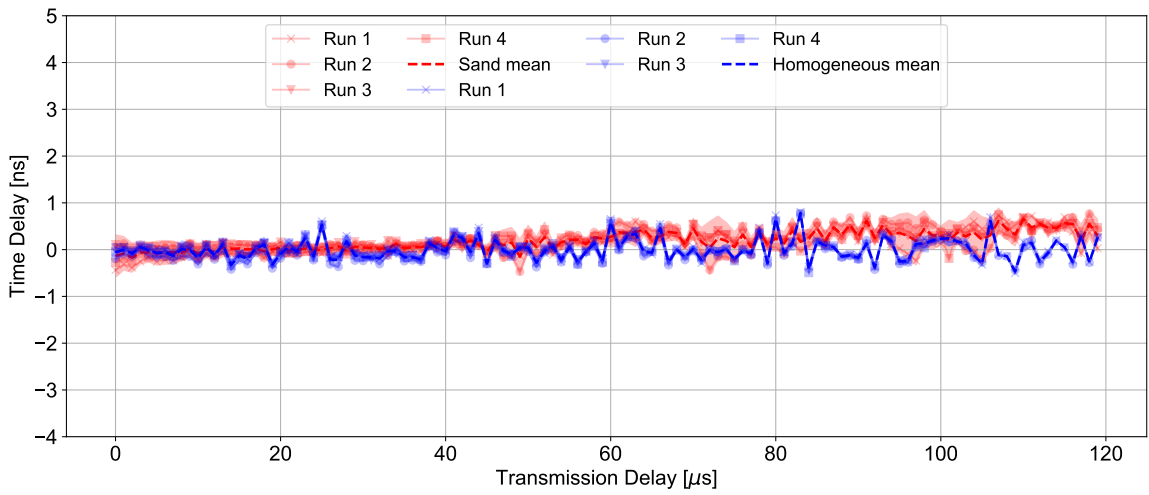


Figure 3.13: Orientation two time delay results for the cement sample with three thin sand layers (red) compared with the homogeneous cement time delays (blue). The average trend of four runs is shown (dashed line) with ± 2 standard deviations highlighted by the shaded region.

3.2.4 Cement with Thin Sand 2 (CS2)

Continuing the investigation of thickness dependency, we now, in addition to approximately probe-wavelength thick sand layers, decrease the interval between layers to 5 mm. Time delay results for orientations one and two are shown in figures (3.14) and (3.15), respectively.

As with the introduction of any inhomogeneity, by increasing the number of thin sand layers from three to seven, we accordingly increase the linear attenuation the probe wave experiences. As our experiment relies on the probe wave as a measurement apparatus, a weaker probe wave (due to increased linear attenuation) leads to a lower S/N, as is the case here. Nevertheless, observations can still be made confidently, such as the slight increase in time delay values in orientation two, which follows a similar characteristic as in the previous thin sand sample and the approximately zero time delay response in orientation one. Therefore, we see an introduction of nonlinearity orientation dependence, which we do not observe in any previous samples.

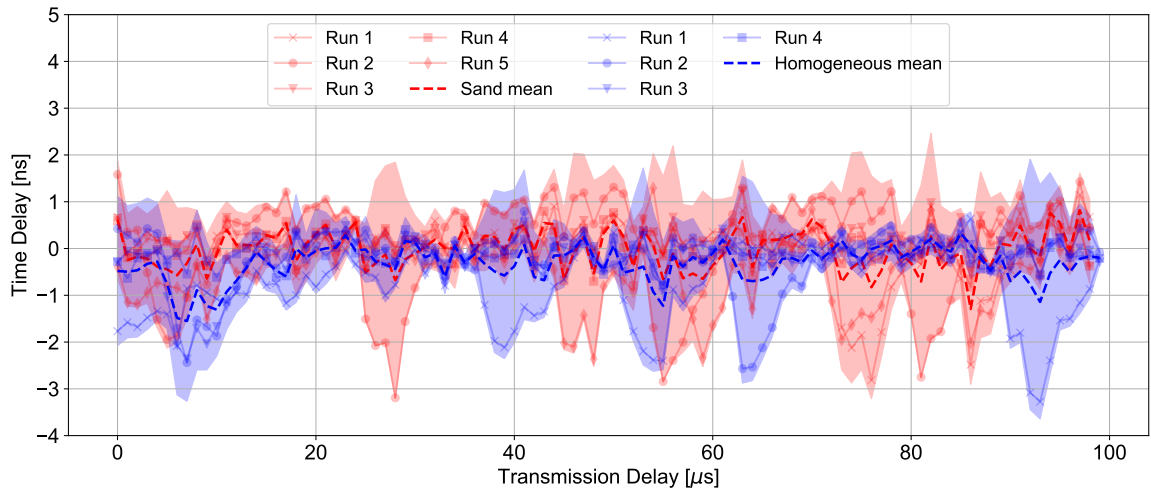


Figure 3.14: Orientation one time delay results for the cement sample with seven thin sand layers (red) compared with the homogeneous cement time delays (blue). The average trend of five runs (four runs) is shown (dashed line) with ± 2 standard deviations highlighted by the shaded region.

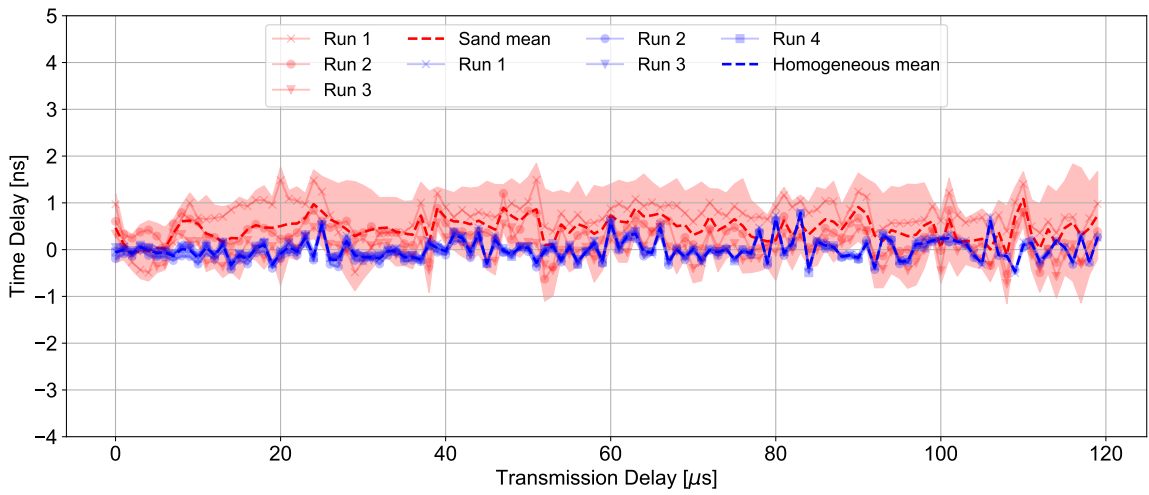


Figure 3.15: Orientation two time delay results for the cement sample with seven thin sand layers (red) compared with the homogeneous cement time delays (blue). The average trend of three runs (four runs) is shown (dashed line) with ± 2 standard deviations highlighted by the shaded region.

3.2.5 Cement with Metal Rods (CR1)

The time delay results from the cement sample with three embedded metal rods are shown in figures (3.16) and (3.17). These samples by far exhibit the lowest S/N due to the manifestation of several high-frequency, high-amplitude time delay values in both orientations. This result is somewhat perplexing as the increase in linear attenuation due to the embedded rods is expected to be small as the rod's spatial extend is limited. That being said, the strong velocity contrast between the cement and the rods will cause the reflection of more energy back towards the source and therefore a weaker signal at the receiver. Relying on the mean trends for observations, while noting the varying standard deviations, we see negligible differences in time delay values compared with that of the homogeneous cement, except for the aforementioned high-amplitude values.

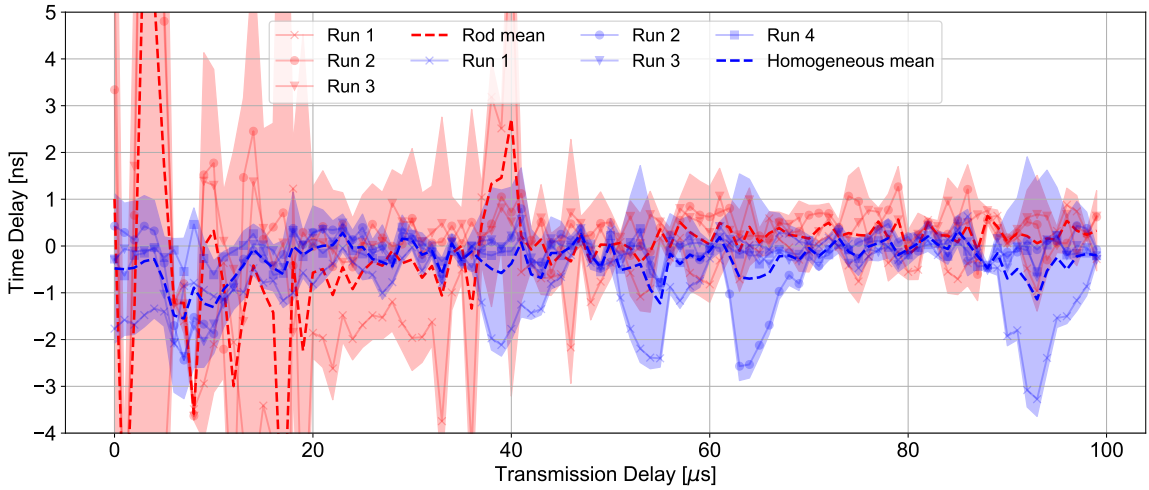


Figure 3.16: Orientation one time delay results for the cement sample with metal rods (red) compared with the homogeneous cement time delays (blue). The average trend of three runs (four runs) is shown (dashed line) with ± 2 standard deviations highlighted by the shaded region.

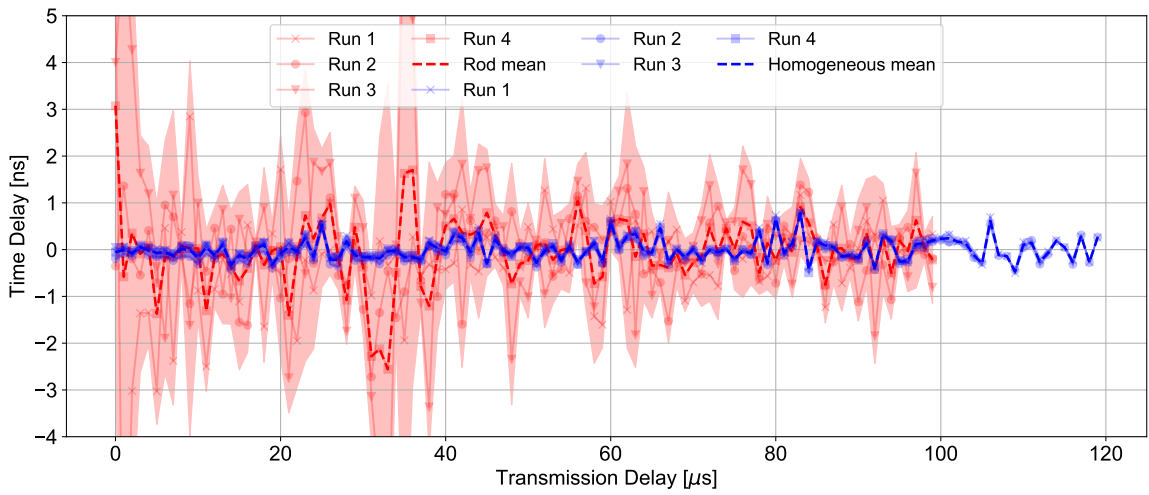


Figure 3.17: Orientation two time delay results for the cement sample with metal rods (red) compared with the homogeneous cement time delays (blue). The average trend of four runs is shown (dashed line) with ± 2 standard deviations highlighted by the shaded region.

3.2.6 Cement with Copper Wires 1 (CC1)

As with the sand layers, we embed a smaller variant of the metal rods, thin copper wires, into cement to further develop the relationship between the inhomogeneity size/separation and the probe's wavelength. Here, we space ten copper wires 5 mm ($\approx \lambda_{pr}$) apart at the centre of the sample. The results in orientations one and two are shown in figure (3.18) and (3.19), respectively.

The most obvious and immediately apparent observation here is the difference in time delay values between the two orientations. We see a marked increase in the time delays in orientation one while the time delays in orientation two remain approximately zero. This result remains consistent over the five (four) runs we complete in orientation one (two).

We complete two of the main objectives we set out to achieve with the synthetic samples with this observation. First, using our TW-DAET experiment, we can observe the presence of embedded inhomogeneities and second, we can deduce the orientation of these inhomogeneities. We will discuss both of these results in more detail in chapter (4)

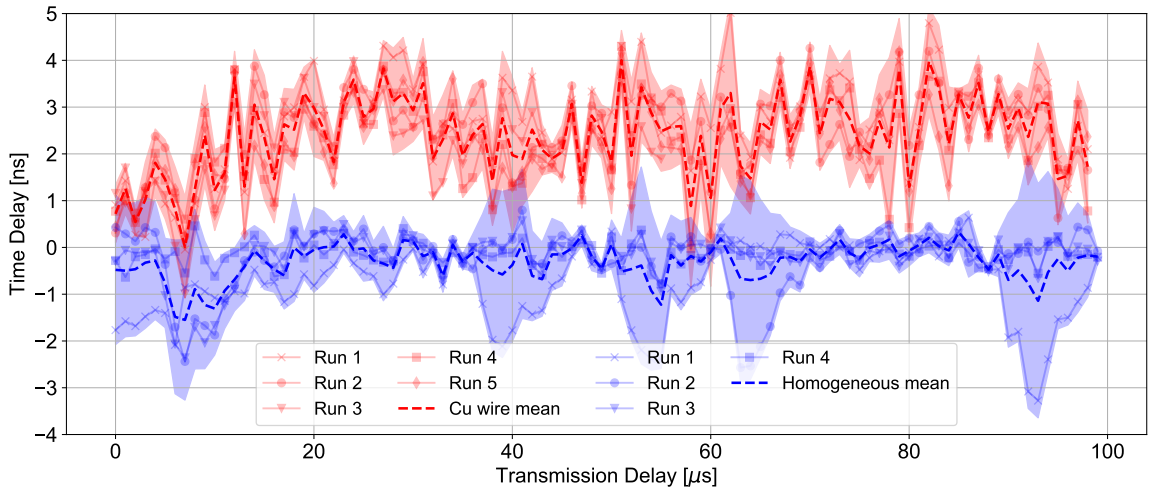


Figure 3.18: Orientation one time delay results for the cement sample with copper wires separated at 5 mm (red) compared with the homogeneous cement time delays (blue). The average trend of five runs (four runs) is shown (dashed line) with ± 2 standard deviations highlighted by the shaded region.

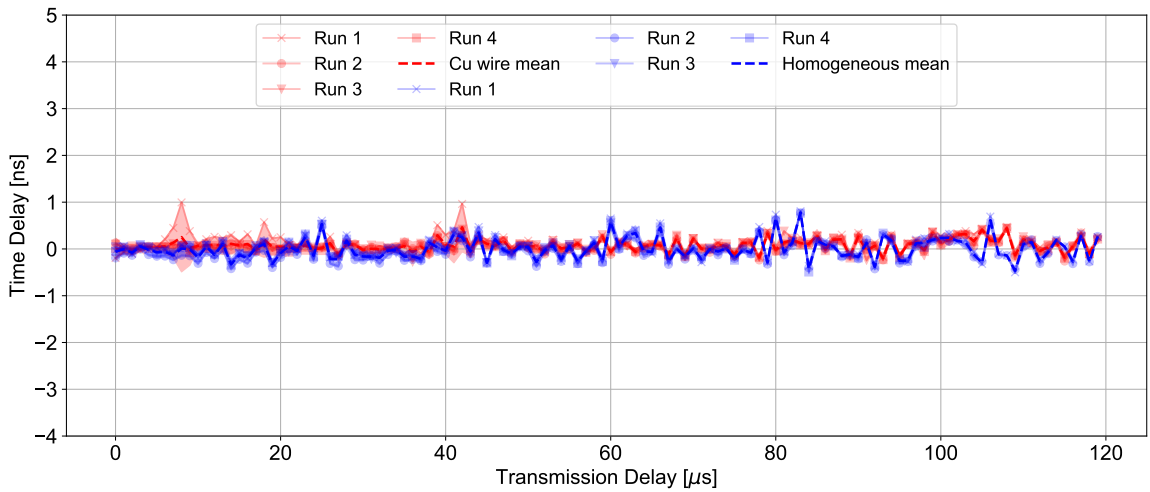


Figure 3.19: Orientation two time delay results for the cement sample with copper wires separated at 5 mm (red) compared with the homogeneous cement time delays (blue). The average trend of four runs is shown (dashed line) with ± 2 standard deviations highlighted by the shaded region.

3.2.7 Cement with Copper Wires 2 (CC2)

To further evaluate the change in time delays with varying inhomogeneity separation, we now create a cement model with ten copper wires spaced at 10 mm ($\approx 2\lambda_{pr}$) placed in the centre of the medium. We show time delay plots from orientations one and two in figures (3.20) and (3.21), respectively.

The most exciting result we observe comes with respect to the previous copper wire sample. Here in orientation one, we see little to no time delay increase contrary to the orientation one results seen above. We will use this result to argue that there is a nonlinearity dependence on the spatial relationship between the inhomogeneity and the probe wave. In addition to the lack of a consistent time delay increase, we also note the presence of several high-amplitude anomalies in orientation one, which we characterize as noise. In orientation two, there is also no change in time delays relative to the homogeneous baseline model. We observe an unusual negative anomaly in the first half of the run one trend in orientation two. We attribute this anomaly, which results in an increase of the standard deviations, to the introduction of deterministic noise.

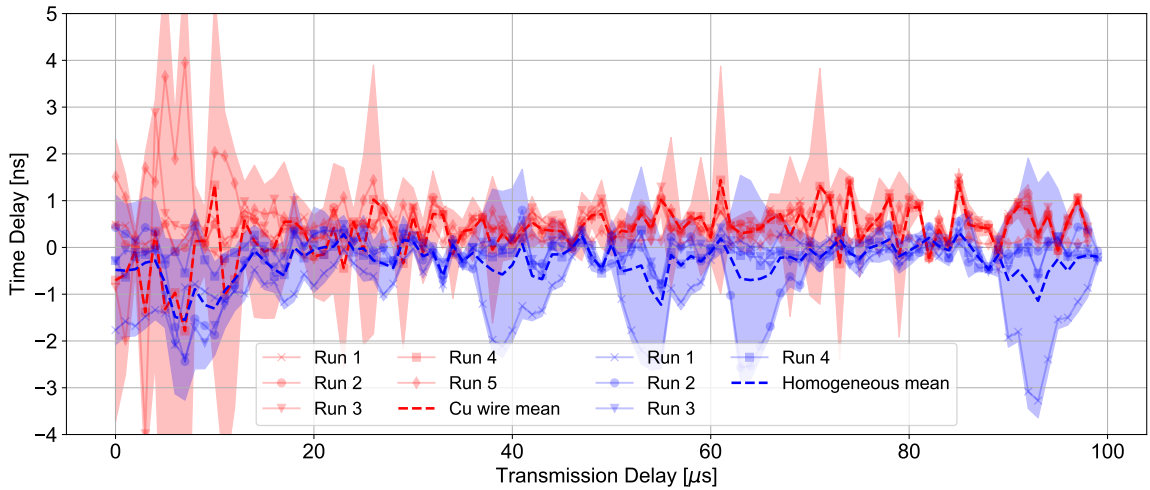


Figure 3.20: Orientation one time delay results for the cement sample with copper wires separated at 10 mm (red) compared with the homogeneous cement time delays (blue). The average trend of five runs (four runs) is shown (dashed line) with ± 2 standard deviations highlighted by the shaded region.

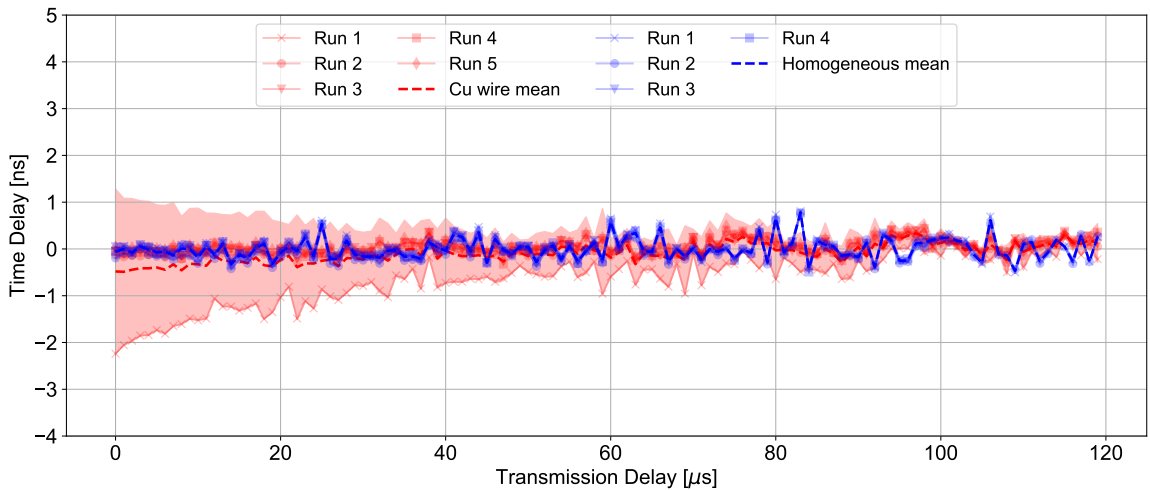


Figure 3.21: Orientation two time delay results for the cement sample with copper wires separated at 10 mm (red) compared with the homogeneous cement time delays (blue). The average trend of five runs (four runs) is shown (dashed line) with ± 2 standard deviations highlighted by the shaded region.

Chapter 4

Discussion

In the following sections, we consider and discuss the results that we present in chapter (3). We define two connections; firstly, the connection between both the experimental branches of this project (section 4.1; section 4.2) and secondly, a connection between our results and the phenomenological models set out in the relevant literature.

4.1 Freeze-thaw Fracturing

This section's discussion examines the project's first experimental branch, namely, freeze-thaw fracturing. As we describe in section (2.2) and later give results for in section (3.1), we subdivide freeze-thaw fracturing into two sections. We base this division on the type of water used to saturate the sandstone samples; tap water and salt-saturated water.

We complete tap water saturation on six sandstone samples (NS1-6), three of which (NS2-5) we present time delay results for in figures (3.2, 3.3 and 3.4) in section (3.1.1). This process aims to induce uniaxial micro-fracturing within the sandstone sample caused by the expansion of pore water upon freezing. Our goal is then to examine the results of TW-DAET on each sample in each orientation to determine if we can

observe both the presence and orientation of the micro-fractures. From examining the figures mentioned above, we observe no significant changes between initial time delays and post-workflow time delays. It is evident that either the sensitivity of our TW-DAET experiment restricts its ability to detect the micro-fractures we induce or the freeze-thaw fracturing workflow with tap water fails to induce any significant uniaxial micro-fracturing. Considering results from both the literature (e.g., TenCate et al. (2016); Rusmanugroho et al. (2019)) and other sections of this project that speak to the robustness of the TW-DAET setup we employ, our results support the latter conclusion.

As we stated in section (2.2.1), instead of saturating multiple sandstone samples as in the case seen previously, we now saturate, with salt water, one model (NS5) numerous times. The objective of this process is to progressively (over four iterations) induce uniaxial micro-fracturing caused by both the expansion of the salt-saturated water upon freezing and the expansion of salt crystals during subsequent drying.

In figure (4.1), we show time delay trends collected in each orientation (one: left column; two: right column) after each freeze-thaw iteration (red) compared to the time delays collected initially (blue). As we begin to discuss in section (3.1.2), several observations manifest with progressive iterations, some prominent and others nuanced.

The most notable observation is the diminishment of time delays (red fill) in both orientations as we advance through the iterations. This decrease is contrary to what we would expect from measuring increases in micro-damage within the sample (Xu et al. (2021)). The reduction of the signal is more prominent in frequencies 1 and 2 (figure 3.1), which in turn tends to emphasize frequency three. There is also evidence for an orientation control on the signal reduction, with orientation two decreasing faster (with progressive iterations) than orientation one. This evidence presents in iteration one, where the orientation two time delays have an overall lower

magnitude and a minimal frequency two component. In contrast, orientation one time delays remain relatively large (albeit still reduced) with a prominent frequency two component.

The second most noteworthy dynamic of the salt-freeze data comes with the reversal of the time delay decrease (blue fill). This reversal occurs with the iteration three orientation one time delays (figure 4.1 left column, row three) where we see a notable increase relative to iteration two. While this increase is slight, the fact that it changes an overall decreasing trend that is consistent throughout speaks to its potential importance when interpreting the underlying physical mechanisms.

Before we interpret these results, we must concede that any conclusions we make should be taken with caution as more experimentation is necessary for further validation. However, as we alluded to in section (2.2.1), these two noteworthy observations, one causing a reduction of time delays (and therefore nonlinearity) and the other causing an increase in time delays, could suggest two underlying physical mechanisms at play. The mechanism causing the reduction in time delays dominates, while the growth mechanism is somewhat secondary. Residual salt left after the drying of the sandstone could be filling a portion of the microstructure (i.e., pore space and micro-fractures), leading to a homogenization of the sample and therefore reducing its elastic nonlinearity (time delays). Concurrently, micro-fractures caused by the aforementioned pore pressure increases cause the elastic nonlinearity to increases. Conceivably, these two mechanisms compete to reduce or increase time delays, with the residual salt regularly prevailing.

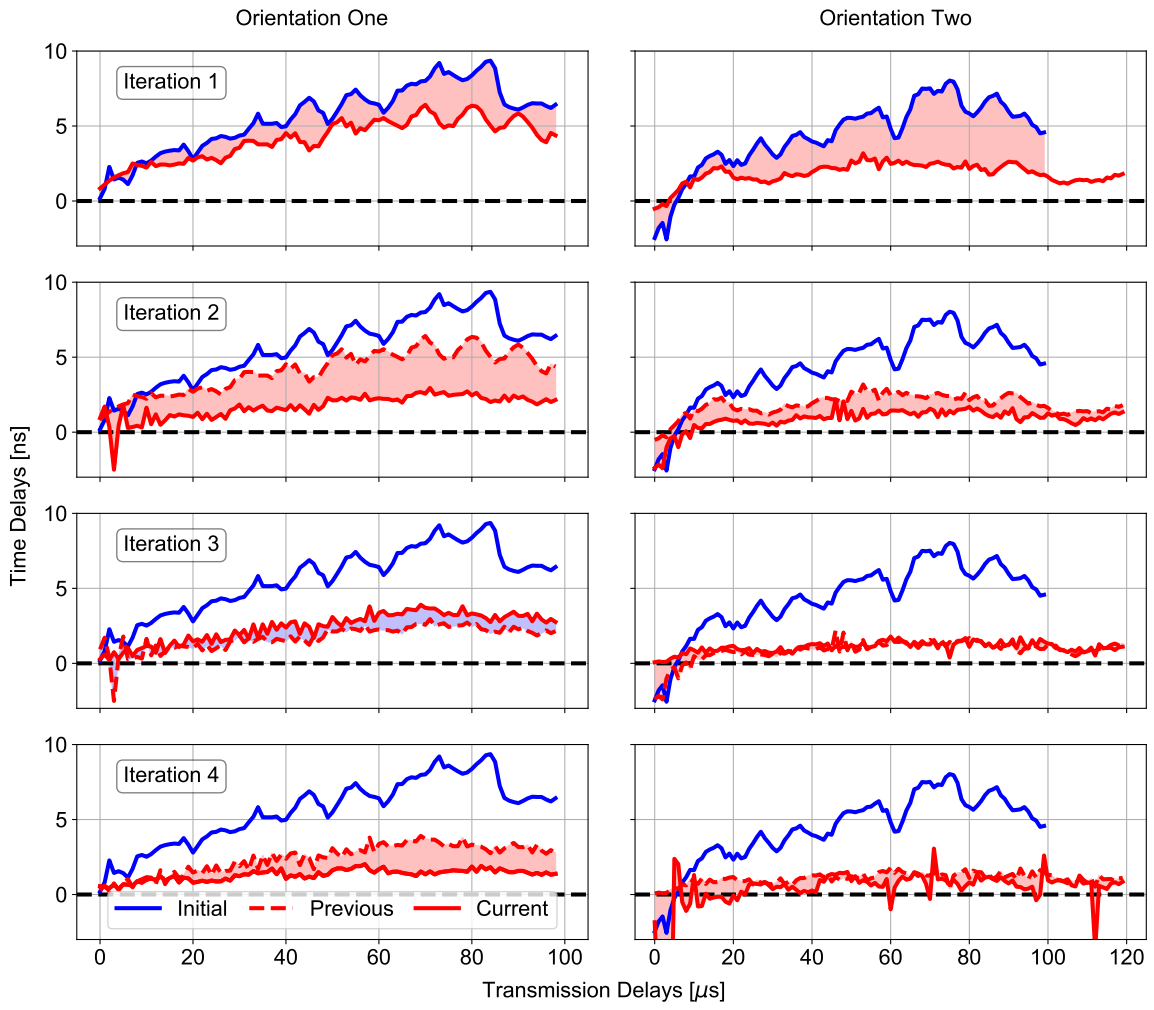


Figure 4.1: Time delay trends from NS5 over iterations (rows) of the salt-freeze workflow in orientation one and two (left and right columns, respectively). Comparison of time delays at the current iteration (solid red) with initial time delays (blue) and time delays of the previous iteration (dashed red). Red and blue fill represent decreases and increases, respectively, relative to the previous iteration.

4.2 Cement Models

We start this section by developing a model that relates the spatial interaction between the pump wave and the embedded inhomogeneities to the time delay response we expect to observe from TW-DAET on the project's cement samples (4.2.1). We then proceed to interpret the time delay trends collected from, first, the sand layer models (4.2.2), and second, the metal cylinder models (4.2.3). In both cases, we attempt to observe evidence of our predicted response and, therefore, evaluate the possibility of imaging the inhomogeneities with TW-DAET.

4.2.1 Expected Nonlinearity Increases

Because the orientation, dimensions and separation of the embedded inhomogeneities (i.e., sand layers and metal cylinders) are known a priori, we can, with respect to the relevant literature, make predictions on the variation of the a-posteriori knowledge (i.e., time delays) we aim to acquire.

As we discuss in chapter (2), the experimental design is such that the transmission of the pump perturbs the elastic properties of the medium in which it travels (high-amplitude \rightarrow high-strain \rightarrow significant perturbation). Conversely, the probe wave's designation is that of a measuring tool and, as such, is not meant to create any substantial changes in the elastic properties of the sample during its transmission (low-amplitude \rightarrow low-strain \rightarrow insignificant perturbation). Considering this design characteristic, it stands to reason that we base any prediction of time delay variations due to the properties of the embedded inhomogeneities (i.e., orientation, dimensions and separation) on the interaction of the pump wave with said inhomogeneities.

Rusmanugroho et al. (2019) show during computational modelling of TW-DAET that when the pump wave's polarization is parallel to the normal of a crack surface,

there is an increase in the time delay response and thus an increase in elastic nonlinearity. Rivi  re et al. (2014) observe experimentally, using standing wave DAET, an increase in nonlinearity when the lowest compressional resonant mode of the cylinder (i.e., the pump) transmits across a fatigue crack. From these two works, we claim that the most significant time delay values we stand to observe will come in the orientation that defines the pump polarization direction perpendicular to the direction in which the embedded inhomogeneities align. More specifically, we claim that when we run TW-DAET on the cement samples with sand layers, we will see the most significant increase in time delays in orientation two (figure 4.2). Alternately, when we run TW-DAET on the cement samples with embedded metal cylinders (rods and wires), the largest time delays will come in orientation one (figure 4.3). Conceptually, one can think of the pump wave attempting to open and close the cracks associated with the cement-sand interface when transmitting in orientation two and move or even strum the metal cylinders when propagating in orientation one. We use the word strum, which is defined as to play a guitar or similar instrument by sweeping the thumb or a plectrum up or down across the strings, intentionally to emphasize our physical interpretation of pump-cylinder interaction.

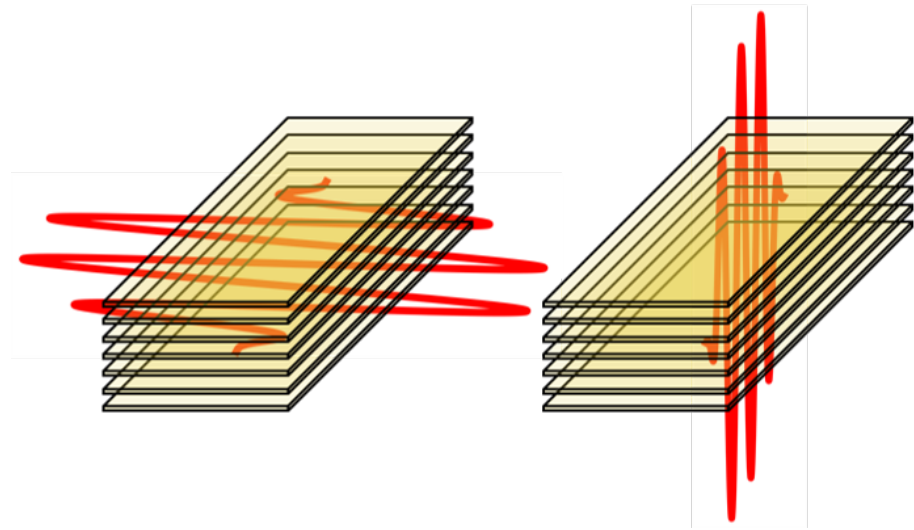


Figure 4.2: Schematic depicting how the pump wave (red) interacts with horizontal unconsolidated sand layers in orientation one (left) and orientation two (right).

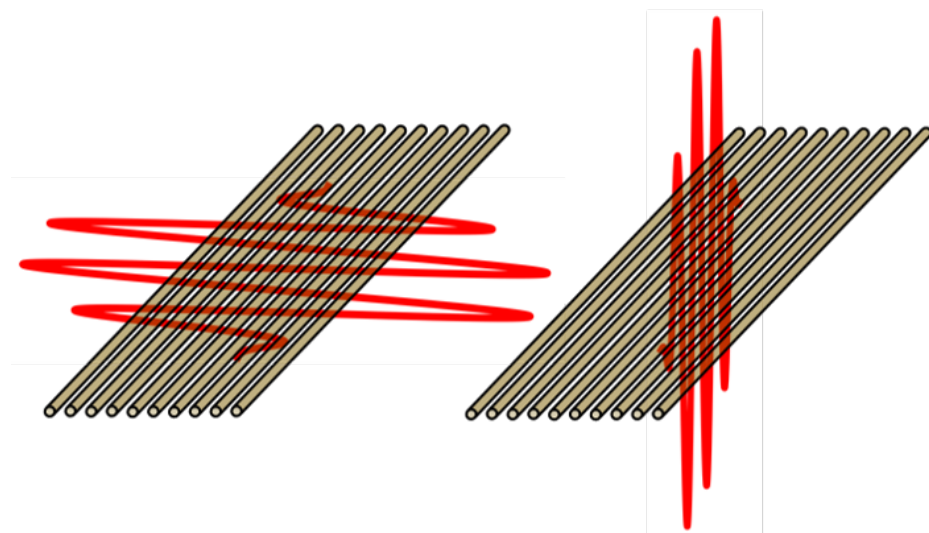


Figure 4.3: Schematic depicting how the pump wave (red) interacts with a network of Cu wires in orientation one (left) and orientation two (right).

4.2.2 Unconsolidated Sand Models

We present the results from the unconsolidated sand layer models (CS1-3) in section (3.2); here, we interpret these time delay values and evaluate whether-or-not we can observe firstly, the presence, and secondly, the orientation of the sand layers using TW-DAET.

We show a schematic of the three models in figure (4.4). CS1 has three 1 cm thick layers of unconsolidated sand (A), CS2 has three 0.5 cm thick layers (B), and CS3 has seven 0.5 cm thick layers, which we also separated by 0.5 cm (C).

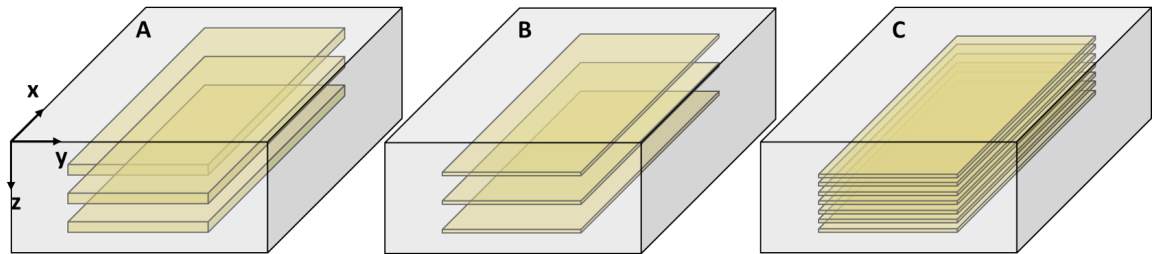


Figure 4.4: A Schematic depicting the three unconsolidated sand layer cement samples; CS1 (A), CS2 (B) and CS3 (C). Note that schematic diagrams are not to scale.

We show the mean time delay trends of the three sand samples (red), along with the homogeneous cement mean (blue), for orientations one and two in figures (4.5) and (4.6), respectively. There is one caveat when examining the differences in orientation we must disclose. The average transmission path distance of the probe wave is 7 cm longer in orientation one relative to orientation two. The longer path distance is significant as the probe will experience an increase in linear attenuation in orientation one, resulting in a noisier time delay response.

In section (4.2.1), we make a claim, which we formulate from relevant previous work, that since the polarization of the pump is parallel to the normal of the sand layers in orientation two, we should expect to see the most significant time delay increases in this orientation. While it is true we see slight increases ($\approx 0.5 - 1$ ns)

in time delays in orientation two for samples CS2 and CS3; we also see an increase of approximately the same magnitude in orientation one for sample CS2. To be consistent with the increases we predict, we expect to see clear-cut differences between orientation one and two. One potential reason for discrepancy stems from the small magnitude of these increases. It is possible that the thin sand layers, which may assimilate with the background cement during the curing process, do not provide a large enough material contrast to facilitate (to a high degree) the nonlinear interaction between the pump and probe, resulting in small time delay values. We, therefore, regard the possibility of determining the orientation of the sand layers unlikely, with the determination of their presence possible, but difficult given the small increases observed.

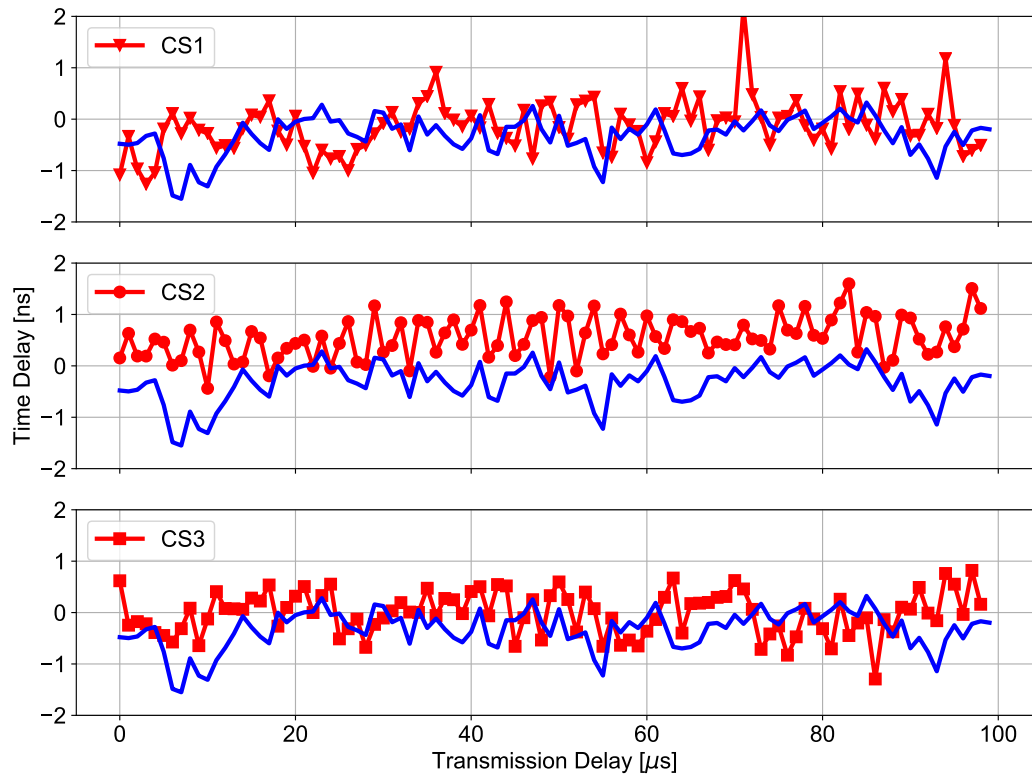


Figure 4.5: Orientation one mean time delay trend comparisons between sand samples (red) and homogeneous cement (blue).

One other interpretation of these results that we elaborate further on in section (4.2.3) attempts to define a relationship between the thicknesses and separations of the inhomogeneities, in this section, sand layers, and the wavelength of the probe. We note that the wavelength of the probe for the sand layer models is approximately 4 mm on average and that we only see increases, albeit small, for samples CS2 and CS3. It is consistent with these results to claim that the nonlinear response (i.e., time delays) is more prominent when the wavelength of the probe is closer to both the thickness of and the separation between the sand layers. This claim opens the possibility of tuning the probe frequency to provide the best opportunity to image the sand layers with TW-DAET. A significant amount of additional experiments would have to be completed to truly validate this claim and is therefore beyond this project's scope and left to future work.

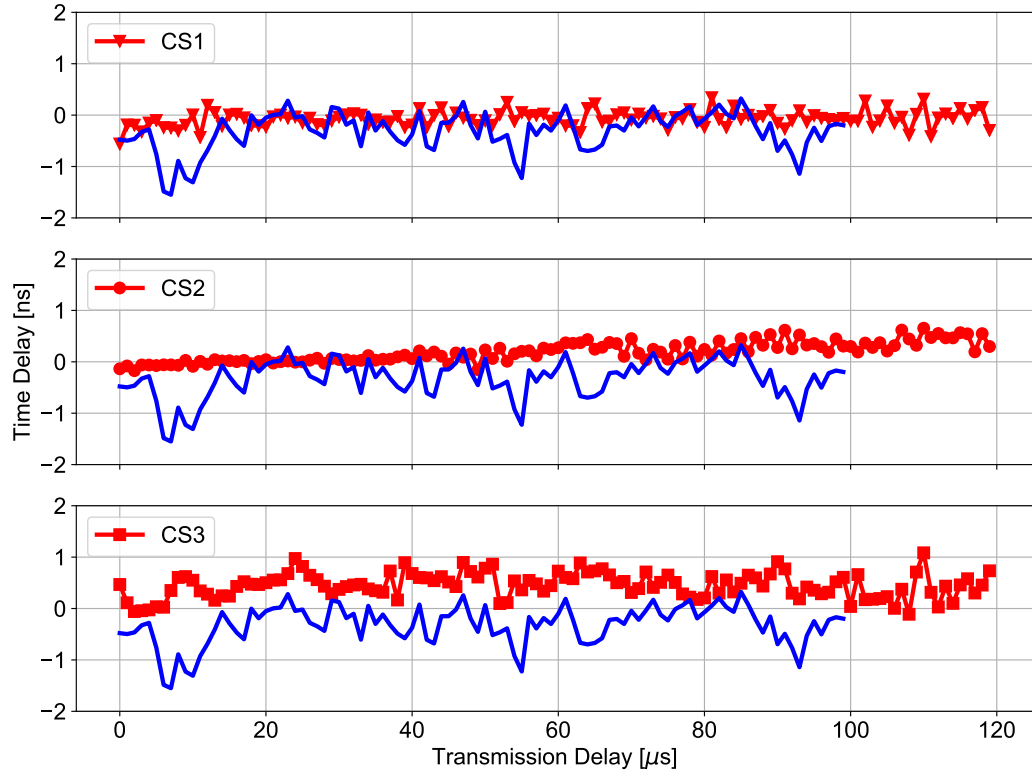


Figure 4.6: Orientation two mean time delay trend comparisons between sand samples (red) and homogeneous cement (blue).

4.2.3 Metal Rod/Wire Models

We give the time delays collected from TW-DAET on the three cement samples with networks of embedded metal cylinders in section (3.2). As in the previous section, we aim to interpret the time delay trends in both orientations to determine the embedded networks' presence and alignment.

We show a schematic of the three samples in figure (4.7). CR1 (D) consists of three metal rods placed centrally within the sample, spaced evenly across the horizontal. CC1 (E) contains a network of ten thin copper wires separated at a 5 mm spacing also centrally positioned. Finally, CC2 (F) is the same as CC1 with only the separation between the wires being increased to 10 mm.

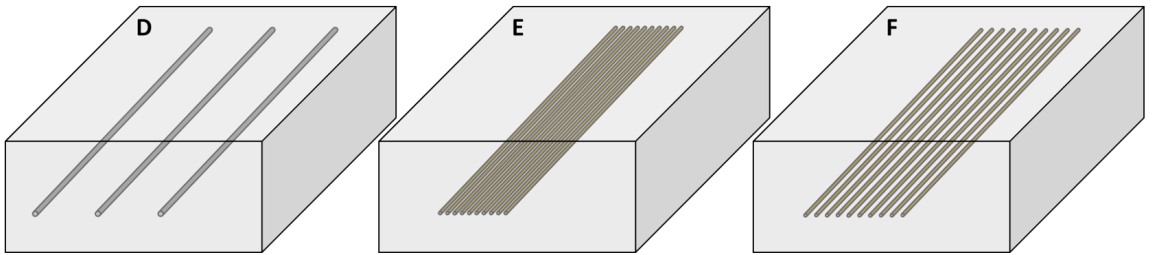


Figure 4.7: A Schematic depicting the three metal cylinder cement samples; CR1 (D), CC1 (E) and CC2 (F). Note that schematic diagrams are not to scale.

We plot the mean time delay trends for all three samples (CR1, CC1 and CC2) for orientations one and two in figures (4.8) and (4.9), respectively. Here, as above, the mean time delay trends collected from the inhomogeneous models are shown in red. We plot, for comparison, the mean time delay trend from the homogeneous cement in blue for each respective orientation.

As we discuss in section (4.2.1), we expect the nonlinear effect we observe from TW-DAET on these samples to be more significant in orientation one relative to orientation two. This expectation is because the pump wave, which causes the perturbation of the medium, is polarized such that its particle motion oscillates across

the metal cylinders (i.e., strumming them) in orientation one. Therefore, we expect the pump wave to interact with more of the inhomogeneities in orientation one, causing a more significant perturbation, which then, in turn, is measured by the probe wave (i.e., time delays).

Here we start discussing and interpreting these time delay trends by distinguishing between CR1 and CC1/CC2. Referring to table (3.1), we see the average standard deviation for CR1 in orientations one and two are 1.1 ns and 0.87 ns, respectively. Comparing these values with that of the same values from CC1 (0.44 ns and 0.055 ns) and CC2 (0.52 ns and 0.28 ns), we note that there is an average standard deviation decrease in orientation one of 60% and 53%, respectively, and in orientation two, a reduction of 94% and 68%, respectively. This means that the time delay trends collected from TW-DAET on CR1 are substantially noisier than that of the time delay trends gathered from the copper wire samples. We allude to the fact in section (3.2.5) that this result is somewhat perplexing as generally, we associate a decrease in the S/N with higher linear attenuation of the probe wave which, because the metal rods have a relatively limited spatial extent, is expected to be small. One reason for the decrease of the CR1 S/N, which also pertains to the probe amplitude, is the high-velocity contrast between the metal rods and the background cement. The amount of energy reflected towards the source transducer of the probe and thus away from the receiver transducer is directly proportional to this contrast. Therefore, this significant contrast reduces the amplitude of the probe signal we record and, in turn causing a reduced S/N of the time delays. Because of this S/N reduction and, therefore, the lack of any statistically significant time delay change between CR1 and homogeneous cement (CH1), we continue our discussion and interpretation in reference to only the copper wire samples (CC1 and 2).

The most significant change we see with the copper wire samples comes with CC1

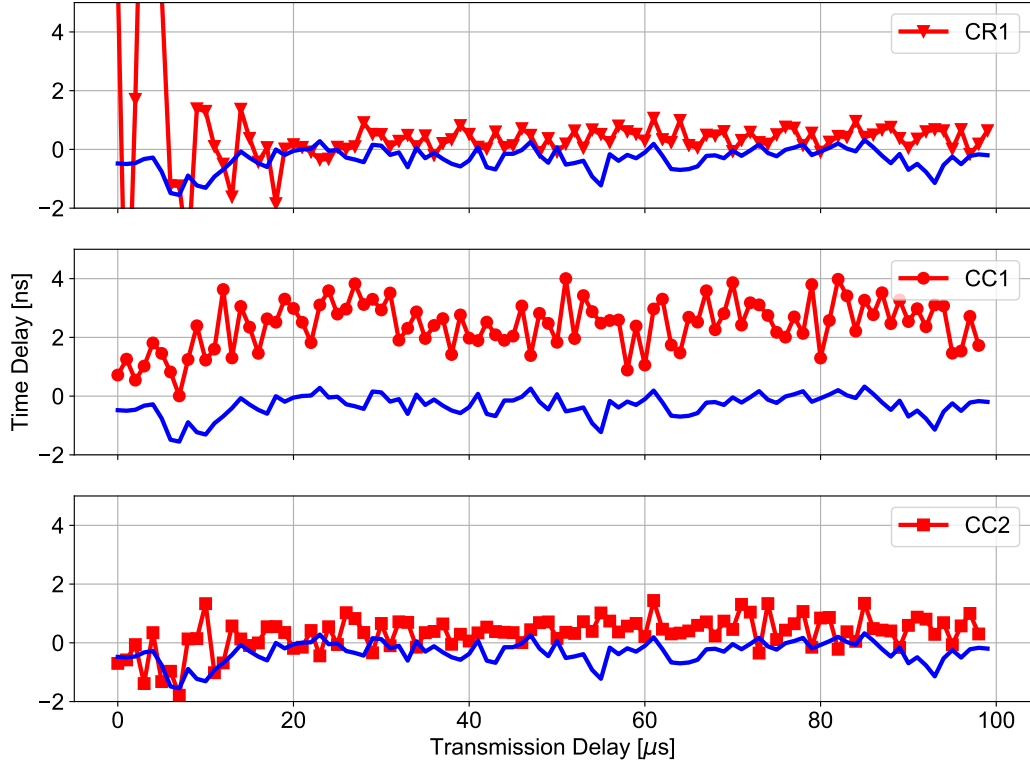


Figure 4.8: Orientation one mean time delay trend comparisons between metal cylinder samples (red) and homogeneous cement (blue).

in orientation one. We observe a mean trend well above that of the mean trend from CH1 in the same orientation, signifying the presence of the copper wire network. While this increase in time delays indicates a change in the medium, in this case, the presence of the copper wires, by no means do we claim that this result is unique to this model. An extensive amount of experimentation is necessary to make this claim and characterize the time delay signatures of different embedded materials. This work would be an extension of this project's results and interpretations. What makes this change even more notable is the lack of any change in orientation two. This result, namely, an increase in orientation one time delays and no change in orientation two time delays, is what we predict in section (4.2.1), and, indeed, helps us achieve the project's primary goal of delineating the alignment of inhomogeneities using TW-DAET.

An almost equally interesting observation is the lack of any time delay change for CC2 in either orientation. While we would expect this persistency in orientation two (collection of CC1 time delays preceded that of CC2), the absence of an increase in orientation one is quite bewildering. Notwithstanding, this result speaks to the potential relationship between the probe's wavelength and the separation between inhomogeneities that we discuss in section (4.2.2). The probe's wavelength is approximately 4 mm on average for the two copper wire samples, and the separation between the wires is 5 mm and 10 mm for CC1 and CC2, respectively. Therefore, the observation of an increase in orientation one for CC1 and no increase in CC2 provides evidence to the claim that there exists a probe wavelength dependency on the TW-DAET response. To our present knowledge, it is worth noting that no such dependence is put forward in the relevant literature. As we alluded to above, completion of future work is necessary to validate this claim further and, therefore, aid future TW-DAET experiments.

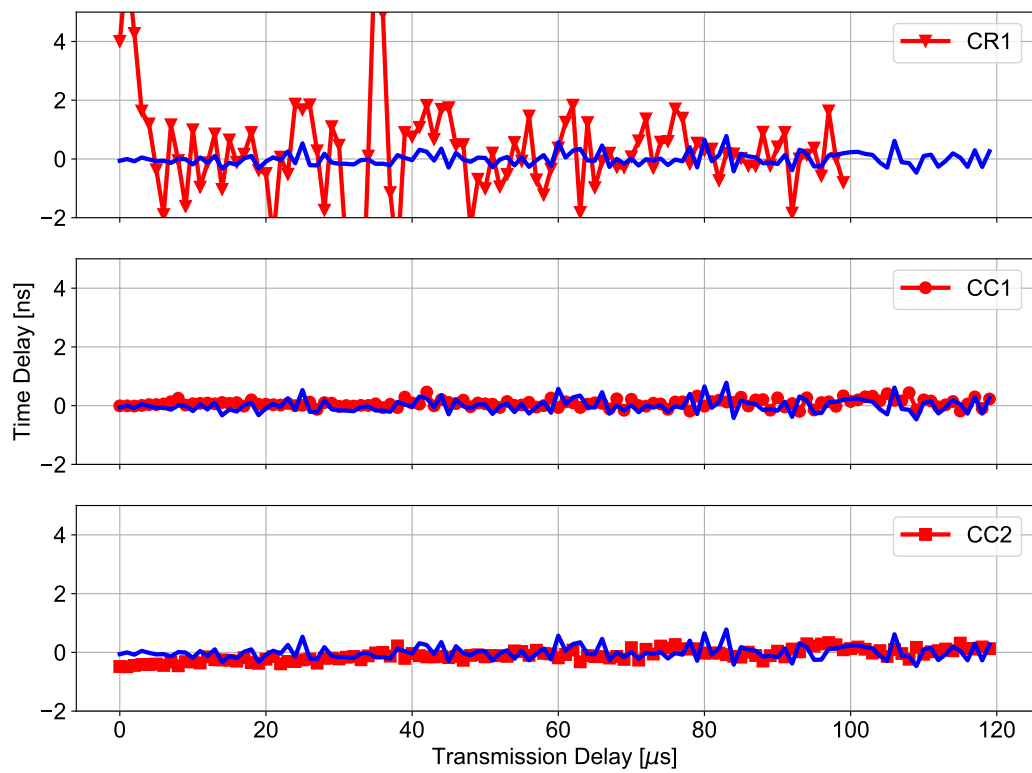


Figure 4.9: Orientation two mean time delay trend comparisons between metal cylinder samples (red) and homogeneous cement (blue).

Chapter 5

Conclusions and Future Work

Dynamic acousto-elastic testing (DAET) that uses a standing wave to perturb the elastic parameters of the medium can detect micro-defects (e.g., micro-fractures) as well as macro-features of the medium (e.g., Haupert et al. (2014)). The issue with this classic variation of DAET comes from initializing the pump field within the sample. To set up a standing wave within a medium, one must know several parameters about that medium *a priori* (e.g., resonance frequency). This requirement becomes a limitation when attempting to use DAET in a real-world environment (e.g., non-destructive testing on concrete infrastructure), as often bringing the medium to resonance is difficult if not impossible. For this reason, using a transient wave pump field to perturb the sample is desirable.

Some experimentation using transient wave dynamic acousto-elastic testing (TW-DAET) is put forward in the literature, but this is by no means as extensive as standing wave DAET. Here we attempt to use TW-DAET to observe both the presence and orientation of multiple types of inhomogeneities. We develop the inhomogeneities in two main branches. One in which we attempt to induce uniaxial micro-fracturing within sandstone samples by subjecting them to freeze-thaw cycles while defining

a maximum principal stress axis. The second branch involves embedding different materials (e.g., unconsolidated sand and metal cylinders), varying the size of and separation between, within cement samples.

The freeze-thaw fracturing branch is further sub-divided based on the type of water (tap water and salt-saturated water) we use to saturate the sample before freezing.

We present and interpret time delay results from the TW-DAET of three sandstone samples (NS3-5), each put through one freeze-thaw cycle with tap water. We observe no significant changes between time delays before and after the freeze-thaw cycle for either of the three samples. For this reason, we conclude that the freeze-thaw process with tap water fails to induce any micro-fracturing. Further to this, we re-define our experimental setup's noise level based on how consistent the time delays remain throughout the process.

We approach the salt-saturated water freeze-thaw process slightly differently than for the tap water case. Instead of subjecting multiple sandstone samples to one freeze-thaw cycle, we now implement numerous freeze-thaw cycles (four iterations) on one sandstone sample (NS5). The time delay results from these four iterations suggest two underlying physical mechanisms at play: one that works to decrease time delays (and thus nonlinearity) and another that increases time delays. We observe that the decreasing mechanism tends to trump the increasing mechanism except during iteration three in orientation one. It is feasible that the cause of the reduction in time delays is residual salt left after drying, which fills the sample's microstructure, causing a homogenization that reduces elastic nonlinearity. Concurrently, micro-fracturing caused by the expansion of saltwater upon freezing and the expansion of salt during the subsequent drying process works to increase the elastic nonlinearity of the sample. Since we observe an increase in time delays in one iteration and one orientation, we claim that we could signify the presence of micro-fractures with TW-DAET; however,

future experimentation is necessary to substantiate this claim. Imaging the orientation of the micro-fractures remains an open question and should be the topic of future studies.

We present time delay trends for six cement samples, three with unconsolidated sand layers (CS1-3), one with three embedded metal rods (CR1) and two with embedded copper wire networks (CC1-2).

We observe slight time delay increases for the sand samples with layer thicknesses of 5 mm (CS2-3), leading to the proposition that we can mark their presence. However, completion of future work is necessary to substantiate this claim further. Since these increases occur in both orientations (orientation one for CS2 and orientation two for CS2 and 3), distinguishing the alignment of the sand layers with TW-DAET remains inconclusive.

The time delays from CR1 show little statistically significant signal, possibly due to large amounts of the probe signal reflecting toward to source transducer caused by the considerable velocity contrast between the metal rods and the background cement.

We observe a significant increase in time delay values from CC1 in orientation one, with no change in time delays in orientation two. This result provides evidence to suggest that using TW-DAET, we can observe both the presence of the copper network and its direction. Compiling more evidence for this should be the topic of future work. Interestingly, there is no time delay increase for CC2 in either orientation. As with the sand layer samples, we observe increases in time delays when the thicknesses (sand layers) or separations (copper wires) are approximately the same as the probe's wavelength. When we increase the separation, we observe no change in the nonlinear response of the sample. This observation suggests a potential nonlinear response dependence on the inhomogeneity thickness/separation; no such dependency is put forward in the relative literature to our present knowledge. Future exploration of

this relationship could aid in the optimization of future TW-DAET experiments. Alternatively, there may be some interactions between the wires we observe with our TW-DAET that do not occur when we increase the separation between them. We leave further development and testing of this idea to future work.

Bibliography

- Baccouche, Y., Bentahar, M., Mechri, C., Novak, A., & el Guerjouma, R., 2017. Nonlinear analysis of damaged metal-based composite plates using guided waves, *Acta Acustica united with Acustica*, **103**, 967–977.
- Benson, P., Meredith, P., Platzman, E., & White, R., 2005. Pore fabric shape anisotropy in porous sandstones and its relation to elastic wave velocity and permeability anisotropy under hydrostatic pressure, *International Journal of Rock Mechanics and Mining Sciences*, **42**, 890–899.
- Bentahar, M., Aqra, H., el Guerjouma, R., Griffa, M., & Scalerandi, M., 2006. Hysteretic elasticity in damaged concrete: Quantitative analysis of slow and fast dynamics, *Physical Review B*, **73**.
- Bentahar, M., Mechri, C., Antonaci, P., Gliozzi, A., & Scalerandi, M., 2019. *Time Domain Analysis of Elastic Nonlinearity in Concrete Using Continuous Waves*.
- Birch, F., 1937. The effect of pressure on the modulus of rigidity of several metals and glasses, *Journal of Applied Physics*, **8**, 129 – 133.
- Bridgman, P., 1912. The liquid and five solid forms, under pressure proceedings of the american academy of arts and sciences, *Proceedings of the American Academy of Arts and Sciences*, **47**, 441–558.

- Delrue, S. & Van Den Abeele, K., 2012. Nonlinear finite element simulation of closed delaminations in composite materials, *Ultrasonics*, **52**, 315–24.
- Delsanto, P. & Scalerandi, M., 2003. Modeling nonclassical nonlinearity, conditioning, and slow dynamics effects in mesoscopic elastic materials, *Physical Review B*, **68**.
- Gallot, T., Malcolm, A., Szabo, T., Brown, S., Burns, D., & Fehler, M., 2014. Characterizing the nonlinear interaction of s- and p-waves in a rock sample, *Journal of Applied Physics*, **117**.
- Gremaud, G., Bujard, M., & Benoit, W., 1987. The coupling technique: A two [U+2010]wave acoustic method for the study of dislocation dynamics, *Journal of Applied Physics*, **61**(5), 1795–1805.
- Gusev, V., Castagnéde, B., & Moussatov, A., 2003. Hysteresis in response of nonlinear bistable interface to continuously varying acoustic loading, *Ultrasonics*, **41**, 643–54.
- Guyer, R. & Johnson, P., 1999. Nonlinear mesoscopic elasticity: Evidence for a new class of materials, *Physics Today - PHYS TODAY*, **52**, 30–36.
- Hamilton, M. F., Ilinskii, Y. A., & Zabolotskaya, E. A., 2004. Separation of compressibility and shear deformation in the elastic energy density (l), *The Journal of the Acoustical Society of America*, **116**(1), 41–44.
- Hamilton, M. F., Blackstock, D. T., & Norris, A. N., 2008. *Nonlinear Acoustics*, p. 263–277, Acoustical Society of America.
- Haupert, S., Rivière, J., Anderson, B., Ohara, Y., Ulrich, T., & Johnson, P., 2014. Optimized dynamic acousto-elasticity applied to fatigue damage and stress corrosion cracking, *Journal of Nondestructive Evaluation*, **33**, 1–13.

Hayes, L. O., Malcolm, A., Moravej, K., & Butt, S. D., 2018. Nonlinear interactions of p and s waves under uniaxial stress, *Proceedings of Meetings on Acoustics*, **34**(1), 045012.

Johnson, P. & Sutin, A., 2005. Slow dynamics and anomalous fast dynamics in diverse solids, *The Journal of the Acoustical Society of America*, **117**, 124–30.

Khajehpour Tadavani, S., Poduska, K., Malcolm, A., & Melnikov, A., 2020. A nonlinear elastic approach to study the effect of ambient humidity on sandstone, *Journal of Applied Physics*, **128**, 244902.

Kharseh, M., 2018. Utilize freezing water to generate energy, *Springer Nature Applied Sciences*, **1**.

Landau, L. & Lifshitz, E., 1986. Theory of elasticity, *Course Theoretical Physics*, **7**.

Pellam, J. & Galt, J., 1946. Ultrasonic propagation in liquids: I. application of pulse technique to velocity and absorption measurements at 15 megacycles, *The Journal of Chemical Physics*, **14**, 608–614.

Renaud, G., Callé, S., Remenieras, J.-P., & Defontaine, M., 2008. Exploration of trabecular bone nonlinear elasticity using time-of-flight modulation, *IEEE transactions on ultrasonics, ferroelectrics, and frequency control*, **55**, 1497–507.

Renaud, G., Callé, S., & Defontaine, M., 2009. Remote dynamic acoustoelastic testing: Elastic and dissipative acoustic nonlinearities measured under hydrostatic tension and compression, *Applied Physics Letters*, **94**, 011905–011905.

Renaud, G., Le Bas, P.-Y., & Johnson, P. A., 2012. Revealing highly complex elastic nonlinear (anelastic) behavior of earth materials applying a new probe: Dynamic acoustoelastic testing, *Journal of Geophysical Research: Solid Earth*, **117**(B6).

- Riviére, J., Renaud, G., Guyer, R., & Johnson, P., 2013. Pump and probe waves in dynamic acousto-elasticity: Comprehensive description and comparison with nonlinear elastic theories, *Journal of Applied Physics*, **114**.
- Riviére, J., Remillieux, M. C., Ohara, Y., Anderson, B. E., Haupert, S., Ulrich, T. J., & Johnson, P. A., 2014. Dynamic acousto-elasticity in a fatigue-cracked sample, *Journal of Nondestructive Evaluation*, **33**(2), 216–225.
- Riviére, J., Pimienta, L., Scuderi, M., Candela, T., Shokouhi, P., Fortin, J., Schubnel, A., Marone, C., & Johnson, P., 2016. Frequency, pressure and strain dependence of nonlinear elasticity in berea sandstone, *Geophysical Research Letters*, **43**, n/a–n/a.
- Rusmanugroho, H., Malcolm, A., & Darijani, M., 2019. A numerical model for the nonlinear interaction of elastic waves with cracks, *Wave Motion*, **92**, 102444.
- Scalerandi, M., Glioza, A. S., Haupert, S., Renaud, G., Ait Ouarabi, M., & Boubenider, F., 2015. Investigation of the validity of dynamic acoustoelastic testing for measuring nonlinear elasticity, *Journal of Applied Physics*, **118**(12), 124905.
- Scalerandi, M., Bentahar, M., & Mechri, C., 2018. Conditioning and elastic nonlinearity in concrete: Separation of damping and phase contributions, *Construction and Building Materials*, **161**, 208–220.
- Sens-Schönfelder, C., Snieder, R., & Li, X., 2019. A model for nonlinear elasticity in rocks based on friction of internal interfaces and contact aging, *Geophysical Journal International*, **216**, 319–331.
- Shkerdin, G. & Glorieux, C., 2009. Nonlinear modulation of lamb modes by clapping delamination, *The Journal of the Acoustical Society of America*, **124**, 3397–409.

Slawinski, M. A., 2018. *WAVES AND RAYS IN SEISMOLOGY Answers to Unasked Questions*, chap. Appendix D On hyperelasticity, pp. 454–455, World Scientific Publishing Co. Pte. Ltd., 5 Toh Tuck Link, Singapore 596224.

TenCate, J., Pasqualini, D., Habib, S., Heitmann, K., Higdon, D., & Johnson, P., 2004. Nonlinear and nonequilibrium dynamics in geomaterials, *Physical review letters*, **93**, 065501.

TenCate, J., Malcolm, A., Feng, X., & Fehler, M., 2016. The effect of crack orientation on the nonlinear interaction of a p wave with an s wave: Modulation of p waves by s waves, *Geophysical Research Letters*, **43**.

Van Den Abeele, K., Carmeliet, J., Cate, J., & Johnson, P., 2021. Nonlinear elastic wave spectroscopy (news) techniques to discern material damage.

Winkler, K. & Liu, X., 1995. Measurements of third-order elastic constants in rocks, *Journal of the Acoustical Society of America*, **100**, 1392–1398.

Winkler, K. & McGowan, L., 2004. Nonlinear acoustoelastic constants of dry and saturated rocks, *Journal of Geophysical Research*, **109**.

Xu, Y., Wang, Q., Jiang, X., Zu, H., Wang, W., & Feng, R., 2021. Nondestructive assessment of microcracks detection in cementitious materials based on nonlinear ultrasonic modulation technique, *Construction and Building Materials*, **267**, 121653.

Zabolotskaya, E. A., Hamilton, M. F., Ilinskii, Y. A., & Meegan, G. D., 2004. Modeling of nonlinear shear waves in soft solids, *The Journal of the Acoustical Society of America*, **116**(5), 2807–2813.

Zinszner, B., Johnson, P., & Rasolofosaon, P., 1997. Influence of change in physical

state on elastic nonlinear response in rock: Significance of effective pressure and water saturation, *Journal of Geophysical Research*, **102**, 8105–8120.